Measurement of the neutron-neutron scattering length using the $\pi^- d$ capture reaction

Q. Chen,[1,*] C. R. Howell,[1] T. S. Carman,[2] W. R. Gibbs,[3] B. F. Gibson,[4] A. Hussein,[5] M. R. Kiser,[1] G. Mertens,[6] C. F. Moore,[7] C. Morris,[4] A. Obst,[4] E. Pasyuk,[8] C. D. Roper,[1,†] F. Salinas,[1,‡] H. R. Setze,[1,§] I. Slaus,[9] S. Sterbenz,[4] W. Tornow,[1] R. L. Walter,[1] C. R. Whiteley,[7] and M. Whitton[4,‖]

[1]*Duke University and Triangle Universities Nuclear Laboratory, Durham, North Carolina*
[2]*Lawrence Livermore National Laboratory, Livermore, California*
[3]*New Mexico State University, Las Cruces, New Mexico*
[4]*Los Alamos National Laboratory, Los Alamos, New Mexico*
[5]*University of Northern British Columbia, Canada*
[6]*University of Tübingen, Tübingen, Germany*
[7]*University of Texas, Austin, Texas*
[8]*Joint Institute of Nuclear Research, Dubna, Russia*
[9]*Rudjer Boskovic Institute, Zagreb, Croatia*

(Received 13 March 2008; published 23 May 2008)

We have determined a value for the $^1S_0$ neutron-neutron scattering length (a_{nn}) from high-precision measurements of time-of-flight spectra of neutrons from the ^{2}H$(\pi^-, n\gamma)n$ capture reaction. The measurements were done at the Los Alamos Meson Physics Facility by the E1286 Collaboration. The high spatial resolution of our γ-ray detector enabled us to make a detailed assessment of the systematic uncertainties in our techniques. The value obtained in the present work is $a_{nn} = -18.63 \pm 0.10$ (statistical) $\pm$ 0.44 (systematic) $\pm$ 0.30 (theoretical) fm. This result is consistent with previous determinations of a_{nn} from the $\pi^- d$ capture reaction. We found that the analysis of the data with calculations that use a relativistic phase-space factor gives a more negative value for a_{nn} by 0.33 fm over the analysis done using a nonrelativistic phase-space factor. Combining the present result with the previous ones from $\pi^- d$ capture gives $a_{nn} = -18.63 \pm 0.27$(expt) $\pm$ 0.30 fm (theory). For the first time the combined statistical and systematic experimental uncertainty in a_{nn} is smaller than the theoretical uncertainty and comparable to the uncertainty in the proton-proton $^1S_0$ scattering length (a_{pp}). This average value of a_{nn} when corrected for the magnetic-moment interaction of the two neutrons becomes -18.9 ± 0.4 fm, which is 1.6 ± 0.5 fm different from the recommended value of a_{pp}, thereby confirming charge symmetry breaking at the 1% confidence level.

DOI: 10.1103/PhysRevC.77.054002 PACS number(s): 21.45.−v, 25.10.+s, 13.75.Cs, 25.80.Hp

I. INTRODUCTION

Charge symmetry breaking (CSB) is mostly due to the difference in the masses of the d and u quarks, which is reflected in the different hadron masses and in the ρ-ω and π-η mixings [1]. The difference between the neutron-neutron (nn) and proton-proton (pp) $^1S_0$ scattering lengths, a_{nn}-a_{pp}, is one of the few quantities that provides a measure of the magnitude of CSB. The value of a_{pp} is measured directly by proton-proton scattering with the main error coming from uncertainties in modeling the electromagnetic effects. The recommended value for a_{pp} is -17.3 ± 0.005 (expt) $\pm$ 0.4 (theory) fm [1]. There have been several proposals to measure a_{nn} directly by scattering neutrons from neutrons [2], and there is work underway for a direct measurement of the nn-scattering cross section using the neutron burst inside a pulsed reactor [3]. Until direct measurements of a_{nn} are made, we must rely on indirect methods. The recommended value [4] for a_{nn} has been based on studies of three-body systems. An impressive number of determinations of a_{nn} have been made using neutron induced deuteron breakup over a wide range of incident energies from 10 up to 130 MeV. However, there are significant discrepancies between the a_{nn} value obtained from neutron-deuteron (nd) breakup experiments. Therefore, it has been argued [5] that the value for a_{nn} should be determined using reactions with only two strongly interacting particles (two neutrons) in the exit channel. Two reactions satisfying this criterion are ^{2}H$(\mu^-, \nu_\mu)nn$ and ^{2}H$(\pi^-, \gamma)nn$. There are no data for the ^{2}H$(\mu^-, \nu_\mu)nn$ reaction. The ^{2}H$(\pi^-, \gamma)nn$ reaction has been studied since 1951 [6], but the first significant results came in 1965 when Haddock *et al.* [7] reported their data for 4200 neutron-gamma coincidence events, which were later analyzed by Salter *et al.* [8] to give a value of $a_{nn} = -16.7 \pm 1.3$ fm. Until our work [9] the recommended value [1] for a_{nn} was based mostly on two experiments done at PSI in Switzerland by the same Lausanne-Zuerich-Muenchen Collaboration. Their first result was from a measurement of the γ-ray energy spectrum of the ^{2}H$(\pi^-, \gamma)nn$ reaction using a high-resolution (720 keV) and high-stability pair spectrometer [10]. This measurement did not completely determine the kinematics of the process, and their systematic uncertainty depended on the accuracy and stability of the

[*]Present address: MCI, Ashburn, VA.
[†]Present address: Bettis Atomic Power Laboratory, West Mifflin, PA.
[‡]Present address: MCI, Clinton, MS.
[§]Present address: Pearl River Community College, Poplarville, MS.
[‖]Deceased.

energy calibration and on the linearity of the spectrometer. They detected a total of 428, 000 γ rays from the pion-deuteron ($\pi^- d$) capture reaction. Their result of $a_{nn} = -18.6 \pm 0.5$ fm, which includes a theoretical uncertainty of ± 0.3 fm, is based on fitting the shape of the measured γ-ray energy spectrum with different theoretical models [11–14]. For their second determination of a_{nn} they made kinematically complete measurements of the neutron time-of-flight (TOF) spectrum of the $^2\mathrm{H}(\pi^-, n\gamma)n$ reaction by detecting the outgoing γ ray in coincidence with one of the outgoing neutrons [15]. The γ rays were detected by either a pair spectrometer or in an array of lead-glass Cerenkov counters. Neutrons were detected using a 100-cm tall $\times$ 100-cm wide wall of plastic scintillator bars of dimensions 10 (width) $\times$ 100 (height) $\times$ 5 (thick) cm^3 each. The wall consisted of two layers of bars with 10 bars in each layer. Each scintillator bar was viewed by a photomultiplier on each end so that the vertical position of the neutron could be determined. In this setup even a modest neutron energy and angular resolution suffice to give a much higher-resolution γ-energy determination than is normally obtained in kinematically incomplete measurements in which only the γ-ray is detected. However, the estimated systematic uncertainty critically depends on the neutron detection efficiency and on the precision of the Monte Carlo (MC) simulation used to fold the point-geometry calculation with the energy and position resolution of the experimental setup. A net 130,000 events (after background subtraction) were compared with the calculations [13], yielding the value $a_{nn} = -18.7 \pm 0.6$ fm [15], which includes a theoretical uncertainty of ± 0.3 fm and is consistent with their earlier result [10].

Determinations of a_{nn} have been made using data from kinematically incomplete (KI) and kinematically complete (KC) nd breakup measurements. There are significant discrepancies in the results for a_{nn} obtained from both types of measurement. The situation for both types of measurements are summarized below.

An average value of $a_{nn} = -18.7 \pm 0.2$ fm is obtained from KI nd breakup measurements reported from 1964 through 1986 [16]. A reanalysis [17] of data from KI measurements using modern rigorous three-nucleon theory gives an average value of $a_{nn} = -15.4 \pm 0.3$ fm, which is 9 standard deviations different from the average of the original results. In addition, a recent KI experiment gives a value of $a_{nn} = -16.5 \pm 0.9$ fm [18].

Kinematically complete measurements of the cross section for the $nn\,^1S_0$ final-state interaction (FSI) were recently made by two Collaborations using very different techniques at 13 MeV [19] and 25 MeV [20]. In addition, these same Collaborations measured the neutron-proton $(np)\,^1S_0$ FSI using the same technique. Both measurements gave a value for the $^1S_0$ np-scattering length (a_{np}) that is consistent with each other and in agreement with the value from free np scattering. However, their results for a_{nn} are significantly different. The value obtained at 13 MeV is $a_{nn} = -18.7 \pm 0.6$ fm [19], whereas at 25 MeV, it is $a_{nn} = -16.3 \pm 0.4$ fm [20]. Because there are no apparent reasons to reject either result, one is left with a dilemma and the prospect of effects that are not included in present three-nucleon calculations.

One possibility for the difference in the value of a_{nn} obtained from the data of kinematically complete nd breakup measurements is the magnetic moment interactions among nucleons [21], which were not included in the three-nucleon calculations used in the above experiments. Recently, the influence of the magnetic moment interactions on the nn and np FSI cross sections in nd breakup was calculated in the rigorous three-nucleon model [22]. The net effect of the magnetic moment interactions on the extracted values of a_{nn} and a_{np} was found to be less than 0.2 fm. It is also possible that 3NF effects cause angle dependence of the nucleon-nucleon (NN) FSI cross section. There is some evidence for such an angle dependence in the value of a_{np} determined from np FSI in pd breakup [23]. Howell [24] argues that discrepancies between data and theory in pp quasi-free scattering (QFS), $nn\,^1S_0$ FSI, and the space-star configuration in nd breakup could be related to a possible broad resonance in the $A = 3$ system [25–27]. However, this explanation is unlikely in view of the results obtained in Ref. [27].

Because of the large variance in the values of a_{nn} obtained from nd breakup measurements, the recommended value of a_{nn} is taken from $\pi^- d$ capture measurements. Until the present work [9], the average value for a_{nn} came from only two $\pi^- d$ capture measurements that were made by the same Collaboration [10,15]. Therefore, we feel it is important to give a more detailed account of our work than was presented in the short article in which our main results were reported [9]. In this article we provide details of the experiment, the analysis and the theory used in our determination of a_{nn} from the $^2\mathrm{H}(\pi^-, \gamma n)n$ reaction. The results previously reported [9] were for an analysis that used theoretical cross sections made with nonrelativistic phase-space factors. Here, we report a_{nn} values obtained using relativistic phase-space factors. The results presented in this article slightly differ (by -0.13 fm) from those in our earlier publication [9] due to two factors. First, the use of relativistic instead of nonrelativistic phase-space factors makes a_{nn} more negative by 0.33 fm. Second, a change in the procedure of normalizing the theoretical calculations to the data results in a_{nn} becoming more positive by 0.20 fm.

II. THEORY

The basics of the theory of the $^2\mathrm{H}(\pi^-, n\gamma)n$ reaction is described in Refs. [28] and [29]. There are two modes of π^- capture, $\pi^- + d \to n + n$ and $\pi^- + d \to n + n + \gamma$. The latter occurs about 30% of the time. The final state contains two neutrons in both cases. In the case of $\pi^- + d \to n + n + \gamma$, the way in which the total momentum is distributed among the two neutrons and the photon is sensitive to the interactions between the reaction products. Because the n-γ interaction is very weak compared to the nn interaction, the nn interaction is the main factor that determines the spectra of the final-state momenta. The momenta of the neutrons can be measured very accurately using the time and position information from a TOF spectrometer. These features make the $^2\mathrm{H}(\pi^-, n\gamma)n$ reaction an excellent choice for measuring the nn scattering length a_{nn}.

The laboratory momenta of the two outgoing neutrons for the reaction $^2\mathrm{H}(\pi^-, n\gamma)n$ are p_1 and p_2, and q is the momentum of the emitted photon. The angle between the photon and the detected neutron is θ_{OA} and θ_{nn} is the angle between the two neutrons. Conservation of momentum and energy gives

$$\vec{q} + \vec{p}_1 + \vec{p}_2 = 0 \tag{2.1}$$

$$qc + \frac{1}{2m}\left(p_1^2 + p_2^2\right) = m_\pi c^2 - B_d - (m_n - m_p)c^2. \tag{2.2}$$

The relative momentum of the two neutrons is

$$\vec{p} = \tfrac{1}{2}(\vec{p}_2 - \vec{p}_1). \tag{2.3}$$

In this work, we measured the momenta of the photon and of one or both neutrons, i.e., we conducted a kinematically complete experiment. For this type of experiment, the differential spectrum (unnormalized) is described by

$$\frac{dN}{dx} \approx J(x)|\langle f|H'|i\rangle|^2 p_1 p_2, \tag{2.4}$$

where x is the variable of interest, the neutron TOF in our case. The phase-space factor $p_1 p_2$ is transformed to the appropriate TOF variable by means of the Jacobian $J(x)$. The H' is the transition operator for radiative pion absorption, which is taken from the nonrelativistic reduction of the Chew-Goldberger-Low-Nambu (CGLN) amplitude for the radiative absorption of a pion by a nucleon [30]. Because we are only interested in neutrons with very low relative momentum (the FSI area in the TOF spectrum), it is sufficient to consider H' to be of the form

$$H' = (A + B\vec{\sigma}\cdot\vec{\epsilon})\exp(i\vec{q}\cdot\vec{r}/2), \tag{2.5}$$

where $\vec{\sigma}$ operates on the proton spinor, $\vec{\epsilon}$ is the polarization vector of the photon, and $\vec{r}/2$ represents the position vector of the proton from the center-of-mass of the deuteron, A and B are constants, and $|A| \ll |B|$ [29,30]. Higher-order corrections to the transition operator were estimated to effect the extracted value of a_{nn} by less 0.01 fm. The transition matrix element $\langle f|H'|i\rangle$ can be written as

$$\langle f|H'|i\rangle = \int d^3r \phi_\pi(r/2)\,\phi_d(r) e^{i\vec{q}\cdot\vec{r}/2}\phi_{nn}^{s(t)}(p, r), \tag{2.6}$$

where $\vec{r}$ is the relative separation between the two neutrons. In Eq. (2.6) $\phi_{nn}^{s(t)}(p, r)$ represents the final state of the two neutrons having a relative separation $\vec{r}$ and a relative asymptotic momentum $\vec{p}$. The superscript $s(t)$ refers to the singlet (triplet) spin state, $\phi_d(r)$ describes the initial deuteron, and $\phi_\pi(\frac{1}{2}r)$ is the initial-state pion wave function evaluated at the position of the proton.

The scattering length a_{nn} enters through the phase shift of the $^1S_0$ part of $\phi_{nn}(p, r)$. The phase shift is determined in the effective range approximation by

$$p\cot\delta_0(p) = -\frac{1}{a_{nn}} + \frac{1}{2}r_{nn}p^2, \tag{2.7}$$

where δ_0 is the phase shift, a_{nn} is the scattering length, and r_{nn} is the effective range.

Because deuterium is an isotope of hydrogen, the strong Stark mixing [31] experienced by pionic deuterium insures that all captures occur in S orbitals. Thus, the only atomic effect on the spectrum comes from differences in atomic energy levels that are small enough to be neglected. The main modification to the wave function of the bound pion from a constant wave function is due to the presence of the neutron. The shape of the modified pion wave function was estimated by using the Born approximation on an optical potential consisting of the π-n amplitude multiplying the neutron density in the deuteron. The P-wave contribution is negligible in this case [32] so only S-wave scattering was used. Therefore ϕ_π is of the form:

$$\phi_\pi(r) \sim 1 + a_{\pi n}\left[\frac{1}{r}\int_0^r r'^2\rho(r')dr' + \int_r^\infty r'^2\rho(r')dr'\right]. \tag{2.8}$$

This function shows a decrease of about 15% at $r = 0$ from the constant at $r = 50$ fm. Therefore, it may safely be believed that higher-order terms in the Born series will not introduce errors in the correction larger that 15%. A zero-range wave function was used in $\phi_{nn}(p, r)$ for the $^1S_0$ neutron-neutron scattering state:

$$\phi_{nn}^{\mathrm{ZR}}(p, r) = \frac{\sin(pr + \delta_0)}{pr}. \tag{2.9}$$

For the zero-range model to be a good approximation, the r_{nn} term must be at least one order of magnitude smaller than the a_{nn} term, therefore,

$$p < \sqrt{\frac{-0.2}{a_{nn}r_{nn}}}. \tag{2.10}$$

If we use $r_{nn} = 2.8$ fm and $a_{nn} = -18$ fm, then $p < 0.063$ fm^{-1}. The corresponding range of the relative energy $E = p^2/M$ of the two neutrons in their center-of-mass system is

$$E < 750\ \mathrm{keV}. \tag{2.11}$$

The individual uncertainties contributing to the extracted a_{nn} under different situations have been discussed in detail in Refs. [11,12] and include uncertainties in the nn-scattering wave function (see Ref. [33]), deuteron wave function, effective range, higher partial waves, and the pionic wave function.

The calculated neutron energy (E_n) spectrum and the angular distribution of the outgoing neutrons from the $\pi^- d \to nn\gamma$ reaction are shown in Figs. 1–3. There are two prominent peaks: the nn FSI peak around $E_n = 2.4$ MeV and the $\pi^- p$ quasi-free capture peak, which is labeled as the QFS peak, around $E_n = 9$ MeV (Fig. 1). As shown in Fig. 1, the neutron yield in the FSI peak increases with increasing opening angle. Also, the total neutron yield is maximum at an opening angle of 180°, see Fig. 3.

In the neutron time-of-flight (NTOF) spectrum the FSI peak is around TOF = 120 ns for a flight path of 2.55 m, whereas the QFS peak is around TOF = 62 ns (see Fig. 2). Other relevant features of the calculated NTOF spectrum are that the neutron yields in the QFS peak are insensitive to the magnitude of a_{nn} and the neutron yields in the FSI peak increases as the absolute value of a_{nn} is increased.

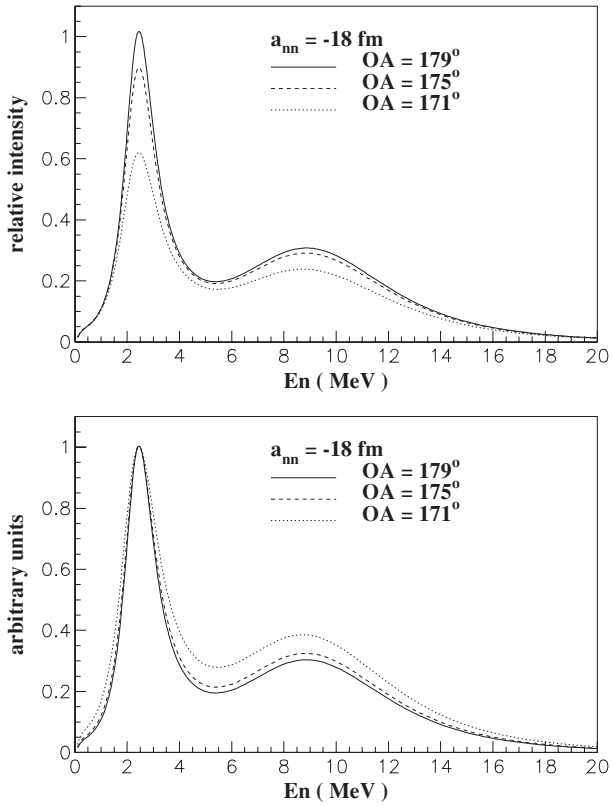

FIG. 1. Calculated neutron energy (E_n) spectra for different opening angle (OA) between the momenta of the emitted γ ray and neutron. (Top graph) Relative intensity of neutrons emitted at three values of OA. (Bottom graph) The E_n spectra are normalized at the QFS peak to compare the shapes of the spectra. All spectra were calculated using $a_{nn} = -18.0$ fm.

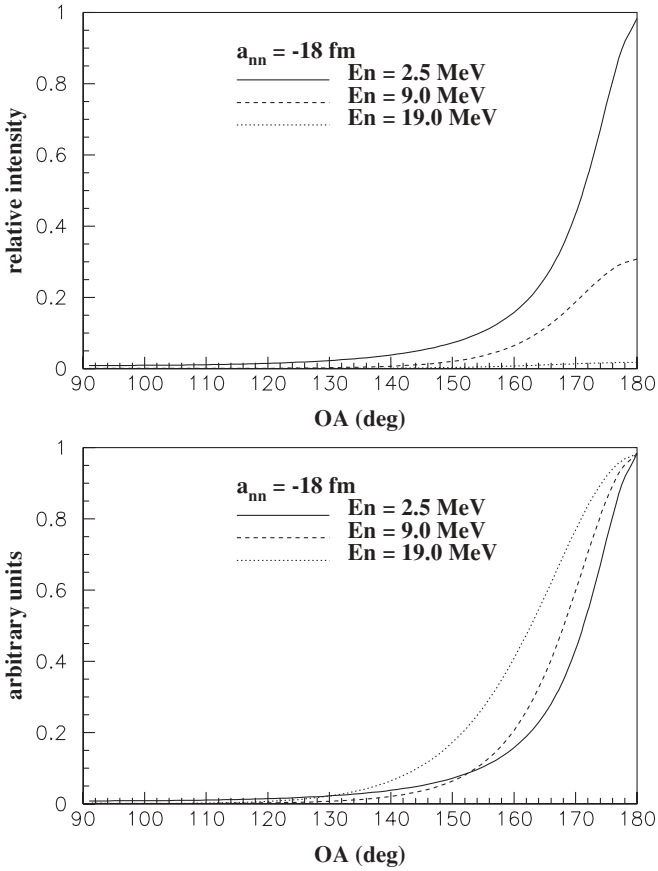

FIG. 3. Angular distributions for different E_n values. (Top graph) The relative intensity at different energies. (Bottom graph) The curves are normalize to have the same intensity at 180° to compare the shapes.

III. EXPERIMENT

The experiment was performed on the low-energy pion beam line at the Los Alamos Meson Physics Facility. The π^- beam was produced by bombarding a rotating carbon target with a beam of 800-MeV protons from a linear accelerator. The average proton beam current on the pion production target was 1 mA. The time structure of the proton beam was 600-μs-long macropulses with a repetition rate of 120 Hz. Each macropulse was composed of 300-ps-wide micropulses with a spacing of 5 ns. The momentum of the π^- beam was selected by transporting the pions through a magnetic chicane [34]. The energy of the π^- beam delivered to the experimental area was 48 MeV.

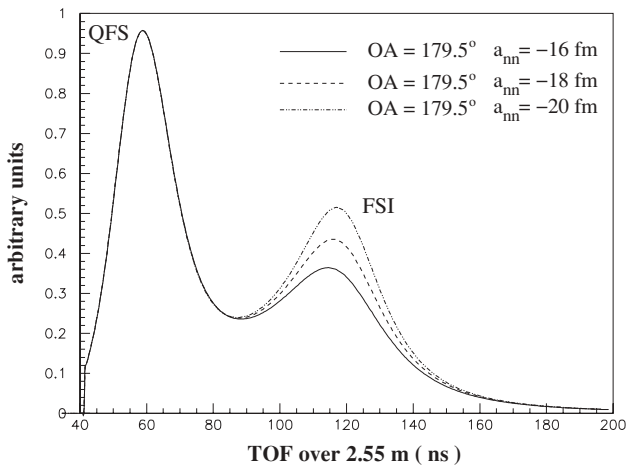

FIG. 2. This figure shows the shapes of the neutron TOF spectra for different values of a_{nn} at the opening angle of 179.5°. All the curves are normalized to have the same area in the QFS peak region.

The layout of the experimental setup is shown in Fig. 4. The cryostat containing the liquid targets was made of stainless steel of wall thickness 0.32 cm and had an outer diameter of 27.5 cm. The energy of the incident π^- beam was degraded from 48 MeV to about 20 MeV by a 4.45-cm-thick rectangular slab of beryllium that was placed 20.3 cm in front of the cryostat. The energy of the π^- beam was further reduced to about 10 MeV by the 0.32-cm-thick iron wall of the cryostat. The origin of our coordinate system is defined as the geometric center of the target chamber, as shown in Fig. 4, and the positive x direction points vertically up (out of the page). The liquid hydrogen/deuterium target was a right cylinder with a diameter of 5.99 cm and a height of 10.16 cm mounted with its axis vertical. The neutrons were detected in an array of 24 liquid scintillators. The front of the array was positioned 250 cm from the center of the liquid deuterium target. The γ rays were

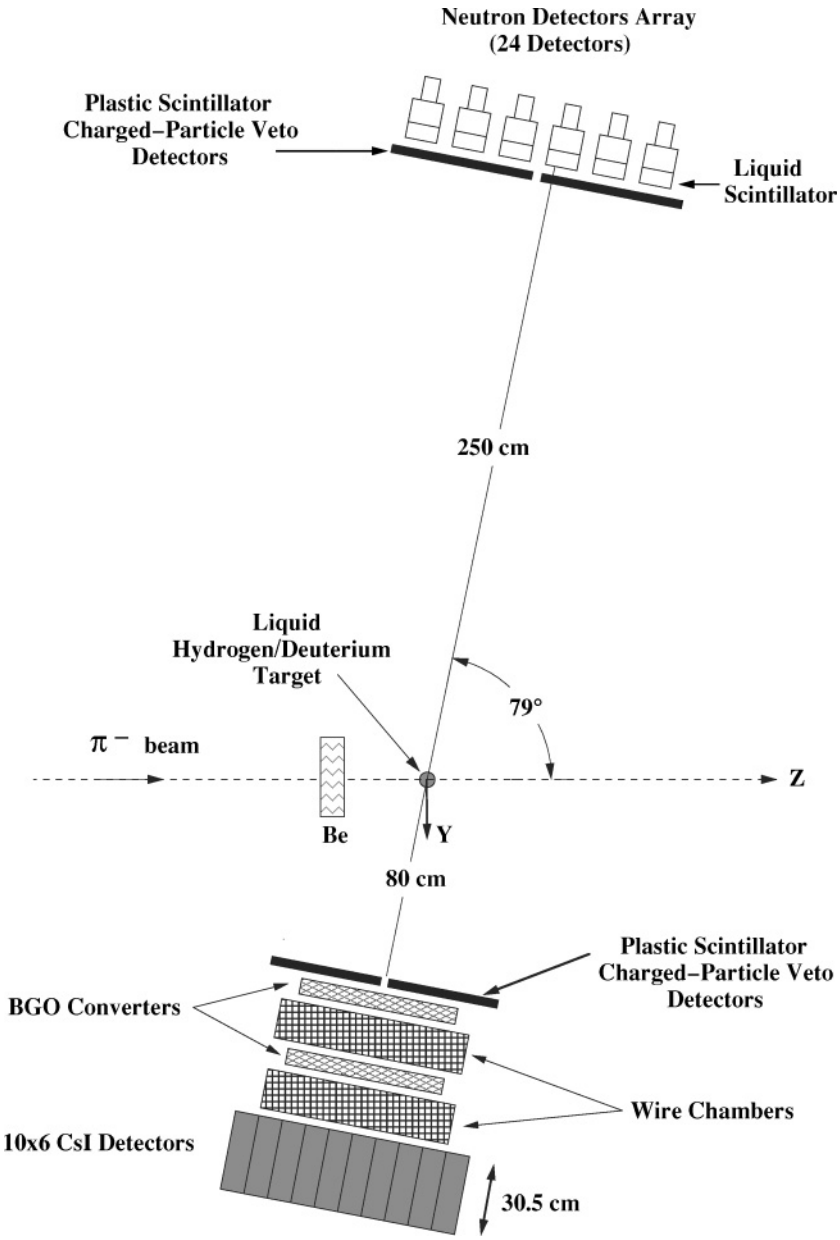

FIG. 4. A schematic view of the experimental layout.

detected in one arm of a neutral meson spectrometer, which was positioned directly opposite of the neutron detector array with the front of the detector stack 80 cm from the center of the liquid deuterium target. The survey of the detector setup was done with a laser tracker system which measured distances to accuracies of about 100 μm. A detailed description of each subsystem is given in this section.

A. Neutron detectors

The schematic of the front view of the neutron-detector array is shown in Fig. 5. The array consisted of four different designs of cylindrically shaped detectors. The A1 type detectors, which were acquired from Argonne National Laboratory (ANL), use liquid organic scintillator BC519 and have an active volume of 12.7 cm in diameter and 1.91 cm in thickness. The A2 type detectors, which were also obtained from ANL, use BC501 scintillator fluid and have active dimensions of 12.7 cm in diameter by 5.08 cm thick. The B type detectors were purchased from the Bicron Corporation and are filled with BC501A liquid scintillator fluid. Their active dimensions are 12.7 cm in diameter by 5.08 cm in thickness. The L-type detectors were obtained from Lawrence Livermore National Laboratory and are filled with NE213 scintillant. The active dimensions of these detectors are 11.43 cm in diameter by 5.08 cm in thickness. The detector types were distributed throughout the array as shown in Fig. 5. With the exception of the B-type detectors, which have a bubble-free design, all other detectors had a nitrogen bubble inside the scintillator cell.

Because the neutron detectors are also sensitive to γ rays, the n-γ discrimination technique was employed to suppress the background events caused by γ rays detected in the liquid

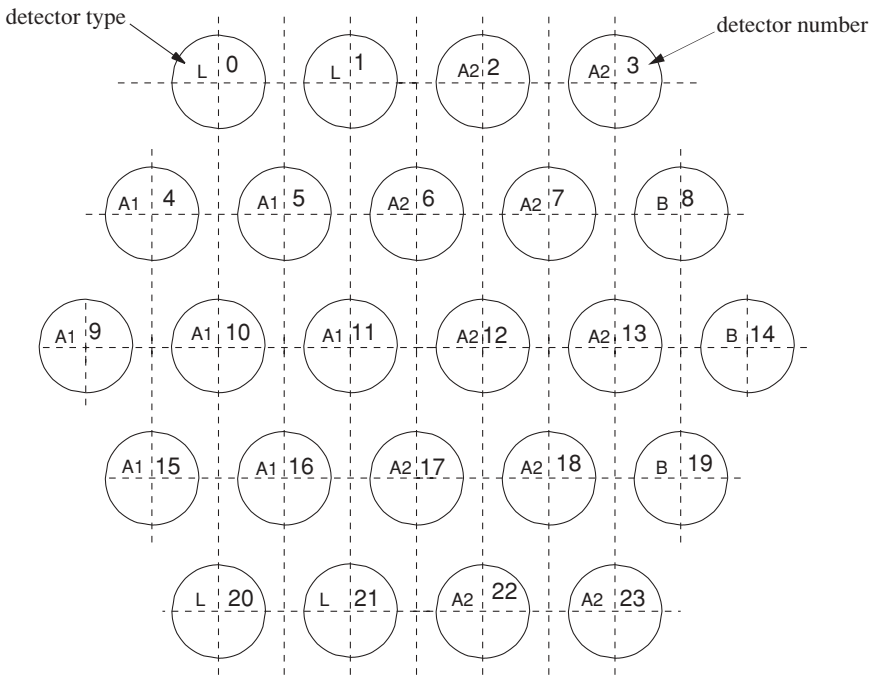

Type	Fluid	Diameter (cm)	Thickness (cm)
A1	BC–519	12.7	1.91
A2	BC–501	12.7	5.08
B	BC–501A	12.7	5.08
L	NE–213	11.4	5.08

FIG. 5. Schematic of the front view of the neutron detector array used in E1286. The detector type is indicated on each detector, and dimensions of the detector types are given in the drawing and in the text. The triangular scale gives the average separation distance between adjacent detectors.

scintillators. An average suppression ratio of 20 to 1 was achieved for the entire array. Plastic scintillator paddles of 6.35 mm in thickness were placed in front of the neutron detectors to veto events caused by charged-particle interactions in the liquid scintillators.

The efficiencies of the neutron detectors over the energy range important for E1286 were measured in a separate experiment at the Triangle Universities Nuclear Laboratory (TUNL) using the ^{2}H$(d, n)^3$He reaction. The cross-section values for the ^{2}H$(d, n)^3$He reaction were taken from the measurements made by M. Drosg [35]. Our measured detector efficiencies were compared to the calculated efficiencies from the NEFF7 code [36,37], which was developed at the Physikalisch-Technische Bundesanstalt (PTB) at Braunschweig, Germany. Comparisons of the measured detector efficiencies to the calculated efficiencies for each detector type are shown in Fig. 6. The deviations of the calculated efficiency curves from our data are less than $\pm 3\%$ for each detector type. The calculated efficiency curves were used in the Monte Carlo simulations of the experiment. An uncertainty of $\pm 3\%$ in the shape of the detector efficiency curve was used to estimate the systematic uncertainty in our determination of a_{nn}.

Because the detection efficiency for neutrons with energies near the detector threshold is very sensitive to small changes in the detector gain, the threshold setting of each neutron detector was regularly checked using a ^{137}Cs and a ^{22}Na γ-ray source. Our data were taken with a detector threshold setting of 157 keVee (electron equivalent energy), which is equal to 1/3 of the scintillator light output for Compton scattering of γ rays from a ^{137}Cs source. This setting corresponds to a neutron energy threshold of about 600 keV. The sensitivity of the efficiency of the four detector types used in E1286 to the threshold setting is shown in Fig. 6 for three settings, 157 keVee ($1/3\times$ Cs), 236 ($1/2\times$ Cs), and 472 keVee ($1\times$ Cs). We found less than 2% variation in the threshold setting during the data accumulation. The uncertainty in the neutron detection efficiency due to this threshold variance was included in the error analysis of our determination of a_{nn}.

B. The γ-ray detectors

The γ-ray detection system was one of the two arms of the Neutral Meson Spectrometer (NMS) constructed at LAMPF [38]. The γ-ray detection arm (see Fig. 4) consisted of three major parts: (1) a single layer of 3.97-mm-thick plastic scintillation paddles to veto event triggers due to charged particles, (2) two planes of bismuth-germanium oxide (BGO) scintillation paddles each followed by four planes of wire chambers (two x and two y), and (3) a stack of cesium iodide (CsI) scintillation detectors.

The BGO paddles were 6.35 mm thick and combined with the tracking wire chambers served as active position sensitive converters. The scintillation light from the BGO

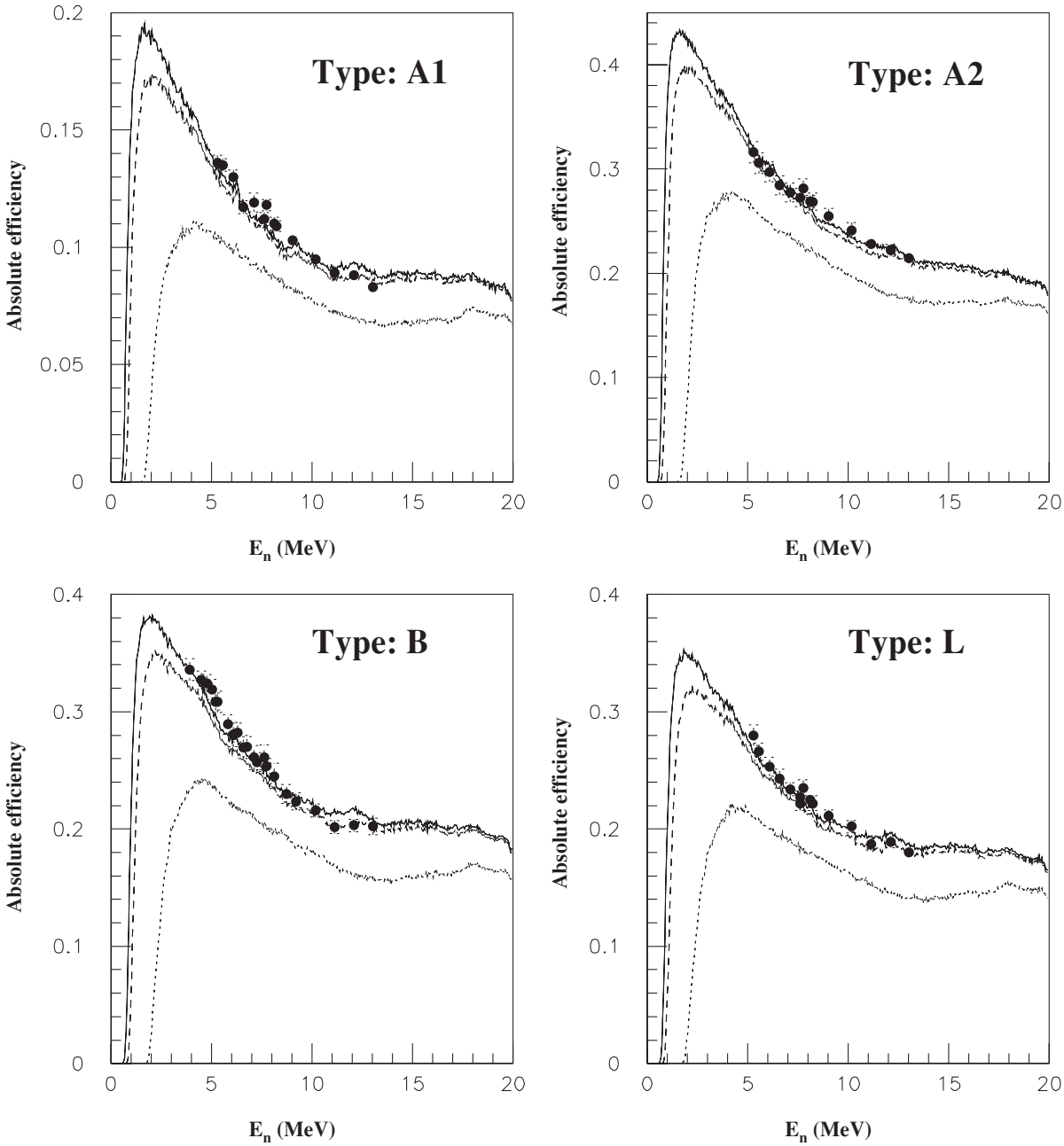

FIG. 6. Plots of the detection efficiency of each neutron detector type used in E1286 as a function of neutron energy. The data points are from measurements made at TUNL using neutrons from the ^{2}H(d, n)^{3}He reaction; see text for description. The error bars on the data represent the combined statistical and systematic uncertainties. The curves are Monte Carlo calculations made with the NEFF7 code for three threshold settings: 157 keVee (solid curve), 236 keVee (dashed curve), and 472 keVee (dotted curve).

crystals provided a measure of the energy deposition by the charged-particle shower in the converter plane, and the subsequent wire chamber planes gave the position of the γ-ray interaction site at the central plane of the BGO detectors. The efficiency of each BGO plane for converting the γ rays to electromagnetic showers was about 30% at γ-ray energies around 130 MeV.

The uncertainty in determining the position of the centroid of the electromagnetic shower in the wire chambers that immediately followed the BGO plane was about 100 μm. With this position resolution in the wire chambers, the uncertainty in our projection of the shower vertex onto the central plane of the BGO detectors was less than 1 mm. The total conversion efficiency of both planes of BGO crystals was about 51%. The energy deposited in the BGO detectors was added to the energy measured in the CsI crystals.

The CsI detector array served as an electromagnetic calorimeter for measuring the energy of the unconverted γ rays and collecting the remaining energy of the charged-particle showers produced in the BGO converter planes. In addition,

it provided the time reference signal for the neutron TOF measurements. The array was a stack of 10 detectors wide × 6 detectors high. Each crystal had a 1° taper in the horizontal direction so that both ends of the array approximately subtended the same solid angle from the center of the deuterium target. The dimensions of the front and back faces of each crystal were 3.58 inches wide × 4.00 inches high and 4.00 inches wide × 4.00 inches high, respectively. All crystals were 12 inches thick.

C. Electronics and data acquisition system

The timing signal for each neutron detector was generated using a constant fraction discriminator (CFD). The threshold settings on the CFDs corresponded to about 80 keVee, which is about one half of the energy threshold used in the data analysis. The pulse shape of the anode signal was used for $n\gamma$-particle identification. The fraction of the total charge of the anode signals that resides in the tail of the pulse was determined by integrating each anode signal with two ADCs, one that integrated the charge in the first 30 ns after the leading edge and another one that integrated the charge in the entire pulse out to 400 ns.

Leading-edge (LE) discriminators were used to generate a timing signal for each CsI detector. In addition, the anode signals from all 60 detectors were summed and fed into a LE discriminator to generate a common timing signal and to set the γ-ray energy threshold of the common timing signal. The CsI detector dynode signals were used for the γ-ray energy measurement. The event trigger signal was generated by the coincidence between the CsI common timing signal and the logical OR (i.e., the output is true if at least one input is true) of the timing signal from any one of the neutron detectors. The coincidence window was 450 ns wide. In addition, the event trigger signal was vetoed by the logical OR of the timing signals from the plastic paddles in front of the neutron detector array and from those in front of the γ-ray detector arm.

D. Determination of finite-geometry effects using the ^{1}H(π^-, $n\gamma$) reaction

Comparisons of spectra accumulated with the two-body ^{1}H(π^-, $n\gamma$) capture reaction with those from the ^{2}H(π^-, $n\gamma$)n reaction enable a direct discernment of kinematic broadening from finite-geometry effects. The same target cell was used for the measurements made with both reactions. Comparisons of some histograms accumulated with the hydrogen and deuterium targets are shown in Figs. 7 and 8. These comparisons clearly indicate that the shapes of the spectra accumulated for the ^{2}H(π^-, $n\gamma$)n reaction are dominated by three-body kinematics rather than finite-geometry detector resolution effects as is the case for the hydrogen-target data.

The histograms accumulated for the ^{1}H(π^-, $n\gamma$) reaction that are shown in Figs. 7 and 8 were used to determine the size of finite-geometry and detector resolution effects for our experimental setup. The focus here is on geometry effects because of the high sensitivity of the shape of the NTOF spectrum from the ^{2}H(π^-, $n\gamma$)n reaction on the opening angle

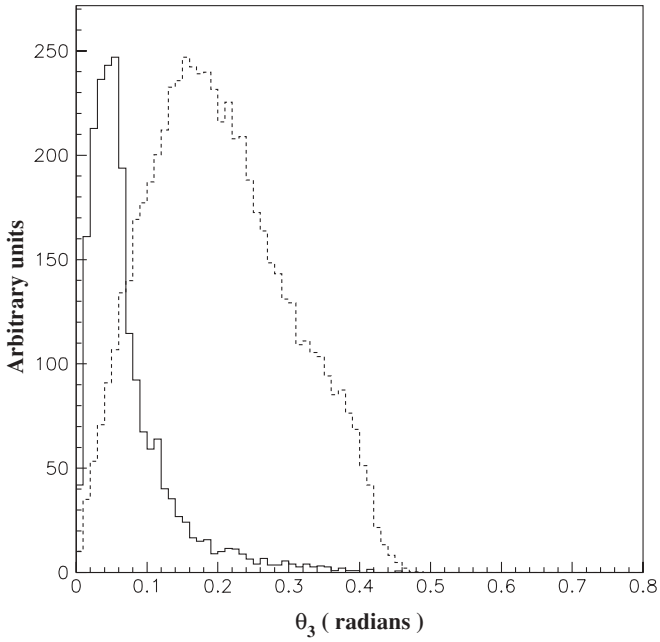

FIG. 7. Measured θ_3 spectra for the hydrogen and deuterium targets after background subtraction. The solid curve is for the hydrogen target and the dashed curve is for the deuterium target.

between the detected neutron and γ-ray. Histograms of the supplemental angle to the n-γ opening angle, θ_3, are plotted in Fig. 7. The dip in the counts of both distributions near $\theta_3 = 0°$ is caused by the reduced solid angle around 0°. The width of the distribution of counts as a function of θ_3 for the ^{1}H(π^-, $n\gamma$) reaction is due mostly to the finite size of the distribution of stopped pions in the target and to the finite size of the neutron detectors. An estimate of the uncertainty in the determination of θ_3 using the full extent of the neutron detectors and the hydrogen target is given by

$$\delta\theta_3 = \sqrt{\left(\frac{R_{\rm det}}{L_n}\right)^2 + \left(\frac{0.5H_t}{L_n}\right)^2 + \left(\frac{0.5H_t}{L_\gamma}\right)^2} = 0.042 \text{ radian}. \quad (3.1)$$

The symbols $R_{\rm det}$, H_t, L_n, and L_γ are the radius of the neutron detector, the height of the target cell, the distance from the center of the target cell to the center of the neutron detector, and the distance from the center of the target cell to the front of the γ-ray detector, respectively. The values used in the estimation are: $R_{\rm det} = 6.35$ cm, $H_t = 5.08$ cm, $L_n = 252.5$ cm, and $L_\gamma = 80$ cm. This coarse estimate is consistent with the observed distribution in Fig. 7 for the hydrogen target. Clearly, the θ_3 distribution for the deuterium target is dominated by reaction kinematics rather than finite geometry effects. As will be shown later, the θ_3 distribution for both reactions are well described by our Monte Carlo simulations.

Because of the high position resolution of the γ-ray detector, about 1.2 mm, it was possible to image the neutron detectors in the plane of the wire chambers using the ^{1}H(π^-, $n\gamma$) reaction with sufficient spatial resolution to observe finite-geometry effects of our setup. The main effect, which is a

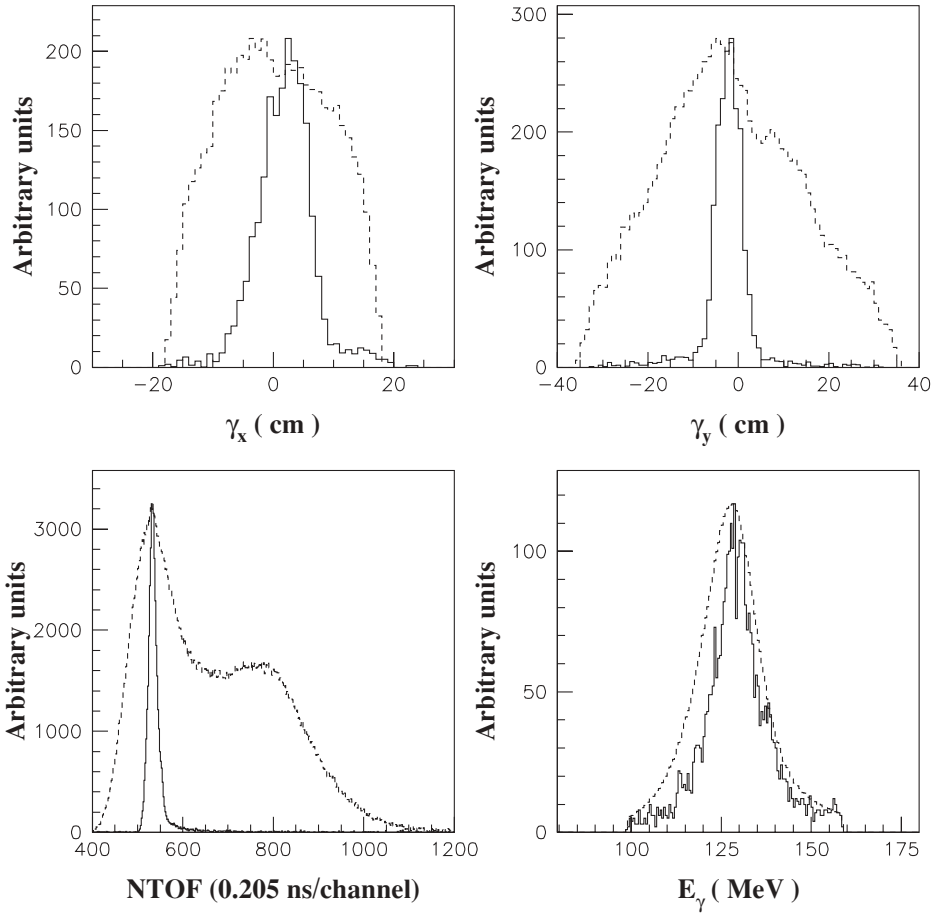

FIG. 8. The experimental γ_x, γ_y, NTOF, and E_γ spectra for the hydrogen target compared to that for the deuterium target for neutron detector 12 after background subtraction. Cuts on θ_3 are not applied. The solid curves are for the hydrogen target and the dashed curves are for the deuterium target. The curves for the two targets have been normalized to the maximum number of counts/channel to enable comparison of the shapes.

broadening of the image, is due to the finite size of the target cell. Also, neutron scattering in the target and in the neutron detector array tend to blur the edges of the detectors in the image.

The vertical (γ_x) and horizontal (γ_y) profiles of the counts distribution of the γ rays coincident with the neutrons detected in scintillator number 12, which is centrally located in the neutron detector array, are shown in the top half of Fig. 8. The solid and dashed curves are distributions that were measured with a hydrogen and deuterium target, respectively. The differences in the width of the γ_x and γ_y distributions taken with the hydrogen target are due mostly to the finite size of the target cell. The γ_x distribution is broader than the γ_y distribution because the height of the target cell is twice its diameter. Using the extreme dimensions of the neutron detector (diameter = 12.7 cm) and the target cell (height = 10.16 cm × diameter = 5.08 cm), the estimated widths of the γ_x and γ_y distributions are $\Delta\gamma_x = \sqrt{[(12.7)(80/252.5)]^2 + [(10.16)(332.5/252.5)]^2} = 14.0$ cm and $\Delta\gamma_y = \sqrt{[(12.7)(80/252.5)]^2 + [(5.08)(332.5/252.5)]^2} = 7.8$ cm, respectively. The first term in each expression is the contribution from the detector dimensions and the second term is the contribution due to the dimensions of the target. The consistency of these rough estimates with the measurements indicates that the contributions from neutron scattering to the γ_x and γ_y distributions are small relative to finite geometry effects.

IV. MONTE CARLO SIMULATION

The value of a_{nn} was determined by fitting the experimental NTOF spectra with theoretical calculations for the $\pi^- d$ capture reaction [11,12,39] as described in Sec. II. For a direct comparison with the experimental spectra, the point-geometry calculations were averaged over the finite geometry of the experimental setup and over the energy, position, and time resolution of the detection system using Monte Carlo (MC) simulations. In addition to accounting for finite geometry and detector resolution effects, the MC simulations included neutron scattering in the liquid target, the cryostat walls, air, and the neutron detector array.

The simulation of each event followed the natural progression of the particles from the reaction site in the target to the detectors. This scheme has the advantage over forced-scattering simulations in that the contributions from each scattering process are internally consistent, thereby avoiding the need for normalization factors between scattering processes, as are often required in forced-scattering simulations. The disadvantage is the low efficiency of the event generator. In the natural flow scheme only a small fraction of the generated incident pions result in detected $\pi^- d$ capture events, as opposed to 100% detection in forced-scattering simulations. The chart in Fig. 9 depicts the flow of events simulated by our MC code.

Comparisons of data and simulations for the two-body $^1\mathrm{H}(\pi^-, n\gamma)$ capture reaction were used to verify that all

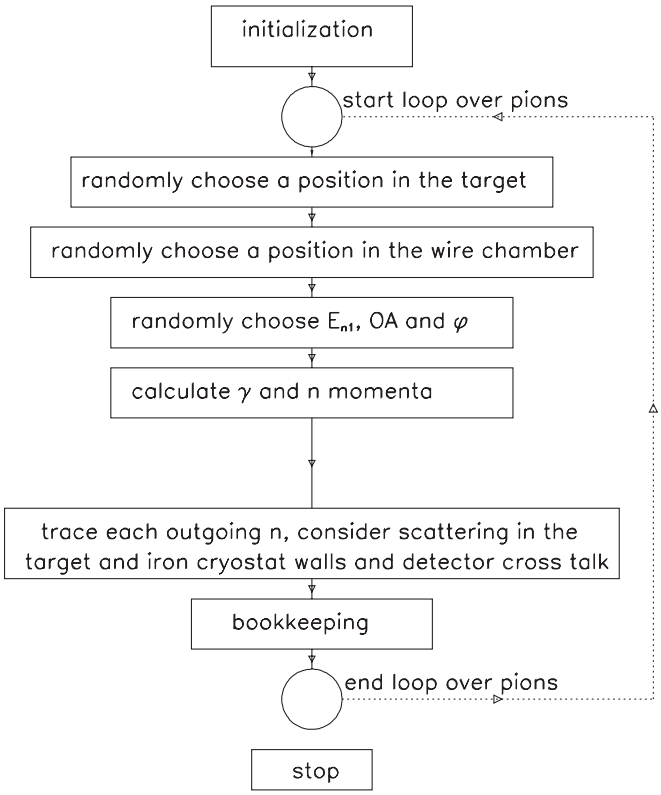

FIG. 9. Flow chart of the Monte Carlo simulation code. The symbol OA is the opening angle between the γ ray and the detected neutron, ϕ is the azimuthal angle of the plane containing the γ-ray and neutron momenta vectors, and E_{n1} is the energy of the detected neutron.

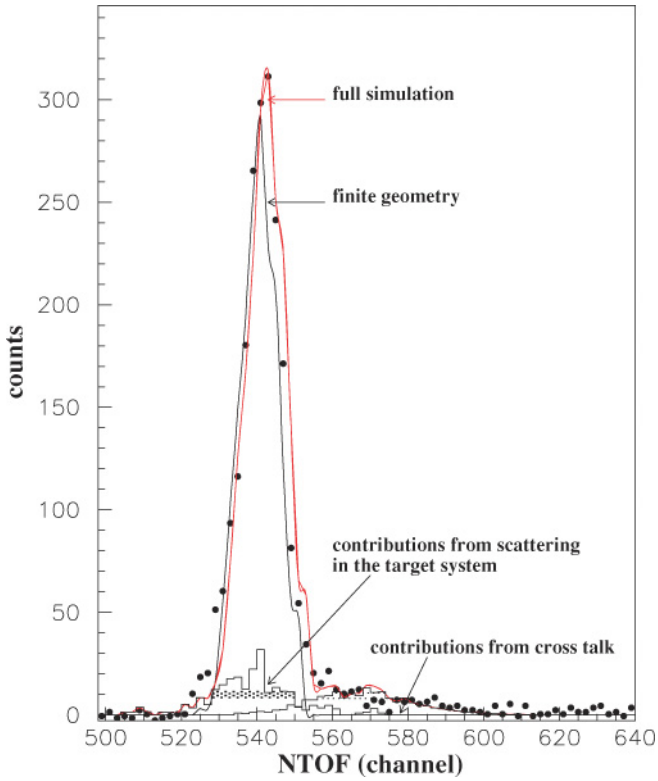

FIG. 10. (Color online) Contributions to the simulated NTOF spectrum. Comparison of experimental NTOF spectrum with the simulated one for the $^1\mathrm{H}(\pi^-, n\gamma)$ reaction. The time scale is 0.205 ns/channel.

significant effects were included in the simulations. An important diagnostic feature of the $^1\mathrm{H}(\pi^-, n\gamma)$ reaction for stopped-pion capture is that the neutron and γ ray are emitted in exactly opposite directions. Calibration runs were made with the target cell filled with liquid hydrogen to accumulate data for the $^1\mathrm{H}(\pi^-, n\gamma)$ reaction. These data were used to determine: (1) the time and energy resolutions of the neutron and γ-ray detectors, (2) the stopped π^- distribution in the target, (3) the amount of out-scattering and in-scattering of neutrons in the liquid target and the cryostat wall, and (4) contributions from neutron scattering between detectors (cross-talk).

Good agreement between the simulation and the $^1\mathrm{H}(\pi^-, n\gamma)$ data were obtained. For example, the relative contributions to the NTOF spectrum due to neutron scattering in the target and the neutron detector array are shown in Fig. 10. The quality of the agreement indicates that all significant effects are included correctly. The geometry parameters were checked by comparing the measured image of each neutron detector in the wire chamber (WC) plane with that of the simulations. From these comparisons, we determined the location of the centroid of the stopped π^- distribution in the hydrogen target.

The same geometry and detector parameters used to describe the data for the $^1\mathrm{H}(\pi^-, n\gamma)$ reaction were applied in the simulations of the $^2\mathrm{H}(\pi^-, n\gamma)\,n$ reaction. In this section we describe how the MC simulations and the $^1\mathrm{H}(\pi^-, n\gamma)$ reaction are used to determine the detector resolution parameters and the finite-geometry effects for our experiment setup. Also included in this section is a description of the simulation of the $^2\mathrm{H}(\pi^-, n\gamma)\,n$ reaction for stopped pions.

A. Detector resolution parameters

The NTOF spectra for the $^1\mathrm{H}(\pi^-, n\gamma)$ reaction was used to determine the time calibration and the time resolution of the γ-neutron coincidences. The peaks in the experimental NTOF spectra for the 8.868-MeV neutrons from the $^1\mathrm{H}(\pi^-, n\gamma)$ reaction have full widths measured at half maximum (FWHM) of 10 to 20 channels (2.05 to 4.10 ns), depending on the detector type; see Fig. 10. The spread in peak widths is mainly attributable to four effects: (1) the finite size of the target and the neutron detectors, which results in the dispersion of the neutron flight path; (2) neutron scattering inside the target material causing dispersion in the energy and flight-path length of the emitted neutrons; (3) neutron scattering in the detector array causing a dispersion in the flight-path length; and (4) the electronic time resolution. The time resolution of each neutron detector was obtained by fitting the 8.868-MeV neutron peak in the NTOF spectrum from the $^1\mathrm{H}(\pi^-, n\gamma)$ reaction with a Gaussian function.

We found that the energy resolution of the γ detectors had position dependency that was different in the vertical and horizontal directions. In the horizontal direction both the

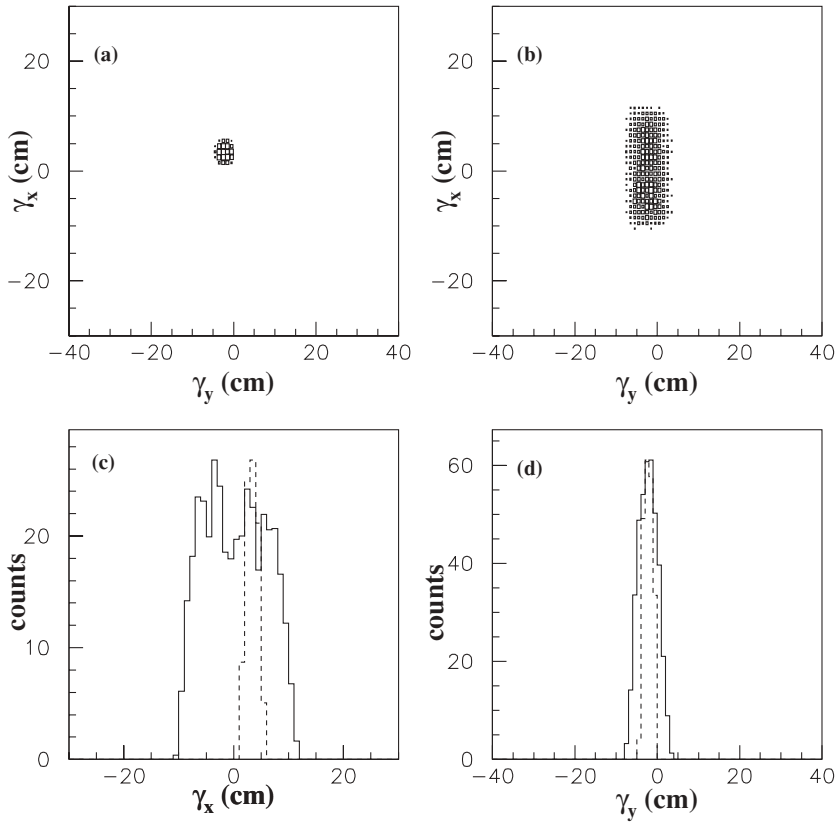

FIG. 11. The γ-ray position spectra for n-γ coincidence events involving neutron detector 12. (a) Plot of the simulated two-dimensional image of neutron detector 12 on the plane of the wire chamber for a point target. (b) Same as (a) except it is for the case of a finite-size target. (c) The projection of the 2D spectra in plots (a) and (b) onto the γ_x axis; the solid curve is the projection of the simulation made with the finite-size target and the dashed curve is for the point target. (d) The same as plot (c) except it is the projection onto the γ_y axis.

centroid and the width of the E_γ peak changed with γ_y. This effect was included in the MC code.

B. Stopped-pion distribution in the target

The energy dependence of the neutron attenuation in the liquid deuterium target causes the shape of the NTOF spectrum to depend on the distribution of the stopped pions in the target. Because a_{nn} is determined from the shape of NTOF spectrum, a reasonably accurate description of the stopped-pion distribution inside the liquid deuterium target is needed to reduce uncertainties in the extracted value of a_{nn}. This shape dependence arises from the effect that neutrons from the $\pi^- d$ capture near the edge of the target cell on the same side as the neutron detectors are attenuated in exiting the target less than those emitted from the opposite side of the target.

The $^1\mathrm{H}(\pi^-, n\gamma)$ reaction was used to make tomographic measurements of the stopped π^- distribution inside the target. The back-to-back neutrons and γ-rays emitted from this two-body reaction were used to make images of a single neutron detector in the WC plane of the γ-ray detector. The sensitivity of our experimental setup to the dimension of the target and the diagnostic capabilities of our instrumentation when used with the $^1\mathrm{H}(\pi^-, n\gamma)$ reaction are illustrated in Fig. 11. The projection of the image onto the vertical axis of the WC plane is sensitive to the stopped pion distribution along the x axis in the target coordinate system (see Fig. 4), and the projection onto the horizontal axis in the WC plane is sensitive to the pion distribution along both the y and z directions in the target but mostly to the z part. The low sensitivity of our setup to the y part of the pion distribution is because the planes of the neutron detector and WC are almost perpendicular to the target y axis. An example of the quality of the fit to the γ-ray vertical position spectrum is shown in Fig. 12. The fit was optimized by adjusting the shape and centroid location of the vertical distribution of the stopped pions within the volume of the target cell assembly. Notice that the vertical part of the stopped pion distribution extends beyond the physical dimension of the target, which is ± 5 cm. This feature of the distribution is due to the liquid hydrogen in the fill tubes at the bottom and top of the target cell. The quality of the fits to the horizontal γ-ray position spectra were similar to those obtained for the vertical part and were used to determine the pion distributions in the z and y directions inside the target.

Because the data taken with the liquid hydrogen target were used to model the stopped π^- distribution in the $\pi^- d$ capture simulations, it was important for the distributions in the two targets to be nearly identical. This condition was met by operating the targets at the same temperature and pressure to constrain the nuclear density of the targets to be the same within 10%. Consequently, differences in the stopped π^- distribution in the deuterium target from that in the hydrogen target were solely due to differences in the π^- beam tune for different runs. The π^- distribution determined using the $^1\mathrm{H}(\pi^-, n\gamma)$ reaction was used in the simulations of the $^2\mathrm{H}(\pi^-, n\gamma)n$ reaction with only modest adjustments made to account for the differences in the beam tune. For example, the centroid of the stopped π^- distribution in the vertical direction

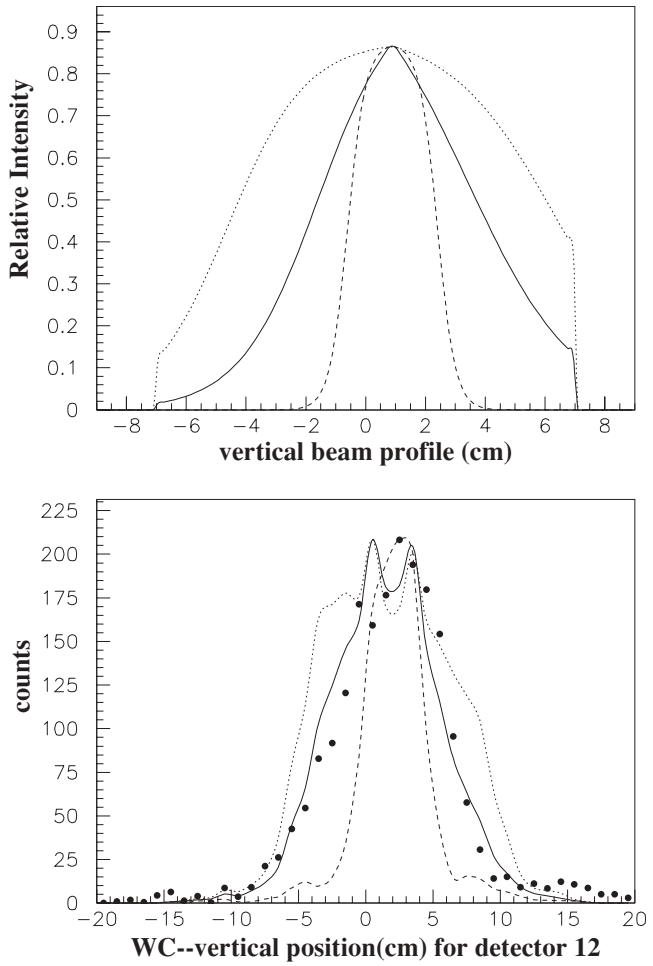

FIG. 12. Comparisons of MC simultions made with different stopped π^- distributions in the liquid hydrogen target to the projection of the measured image of neutron detector 12 onto the vertical axis in the WC plane of the γ-ray detector. (Top) Vertical profile of the stopped π^- distributions used in the MC simulations. (Bottom) Vertical profile of the γ-ray position distribution on the WC plane for neutron detector 12. The curves are the results of simulations made using the stopped π^- distributions in the top panel and the points are data.

was about 1 cm lower with the deuterium target than for the hydrogen target.

C. Neutron scattering in the target and cryostat wall

The experimental NTOF spectra were fitted with the theoretical predictions from the MC simulations using only two adjustable parameters, a normalization factor and a_{nn}. More than 95% of the detected neutrons had energies in the range from 0.5 MeV (just above threshold) to 12.0 MeV. Because the total cross sections for low-energy neutron scatterings are very energy dependent, the shape of the detected neutron energy distribution is critically influenced by the amount of target material the neutrons traverse from the site of their production in the target to the detector array. The neutron attenuation (out-scattering) depends on the dimensions and density of the liquid target, the thickness of the cryostat wall, and the stopped pion distribution inside the target.

Shown in Fig. 13 are predictions of NTOF spectra for three liquid deuterium targets with different radii ($R = 0.0$ cm, $R = 1.78$ cm, and $R = 3.00$ cm). The effects of attenuation in the cryostat wall and in the air between the detector array and the cryostat were omitted in these calculations. The π^- was captured at the center of the target and the neutrons were transported through the half of the target on the side of the neutron-detector array. The influence of the attenuation on the shape of the NTOF spectrum is clearly demonstrated in Fig. 13. The radius of the target used in our experiment was 3.00 ± 0.10 cm. The uncertainty in the target size is due to bulging of the 0.127-μm-thick mylar cell wall under pressure; the mylar cell holds the liquid deuterium/hydrogen. Using the sensitivity calculations presented here, we infer that the 0.10-cm uncertainty in the target radius produces less than 1% uncertainty in the cross section, which corresponds to 0.1-fm uncertainty in our determination of a_{nn}.

The contribution of neutron in-scattering from the cryogenic target and the surrounding materials of the cryostat were included also in the MC simulations. The completeness of the simulations was tested by comparing to the measured spectra for ^{1}H$(\pi^-, n\gamma)$. We found that in-scattering contributed about 3% of the counts in the region of interest in the NTOF spectrum for the ^{1}H$(\pi^-, n\gamma)$, as shown in Fig. 10. The contribution of in-scattering in the ^{2}H$(\pi^-, n\gamma)$ reaction alters the shape of the NTOF spectrum such that it results in a 0.6-fm change in the extracted value of a_{nn}. In addition to accounting for the effects of neutron scattering from the cryogenic target and cryostat, we estimated the contributions due to neutron scattering from the Be degrader, which is located 34.1 cm upstream from the center of the cryogenic target cell. We found that scattering from the Be slab amounts to less than one-tenth of scattering from the other materials considered, i.e., it affects the determined value of a_{nn} by less than 0.06 fm.

D. Effects of cross-talk

For the arrangement of liquid scintillators in our neutron detector array there was a significant probability for a neutron to scatter from a proton or a carbon nucleus in one liquid organic scintillator and then be detected by an adjacent scintillator. This phenomenon is called cross-talk. The effects of cross-talk were included in the MC simulations, so no correction for this effect was subtracted from the measured NTOF spectra. We used the two-body ^{1}H$(\pi^-, n\gamma)$ reaction to determine the contribution of the cross-talk to our measured NTOF spectra. By comparing the simulation to the measured NTOF spectra, we found that the contribution of cross-talk was about 1.5% of the total counts for the ^{1}H$(\pi^-, n\gamma)$ reaction. Neutrons that scatter from one detector into another travel an extra distance before being detected. Therefore, the neutrons detected as a result of cross-talk processes have a longer TOF due to the increased flight path and due to the energy reduction caused by the scattering in the first detector. The effect of cross-talk on the NTOF spectra is larger for detectors

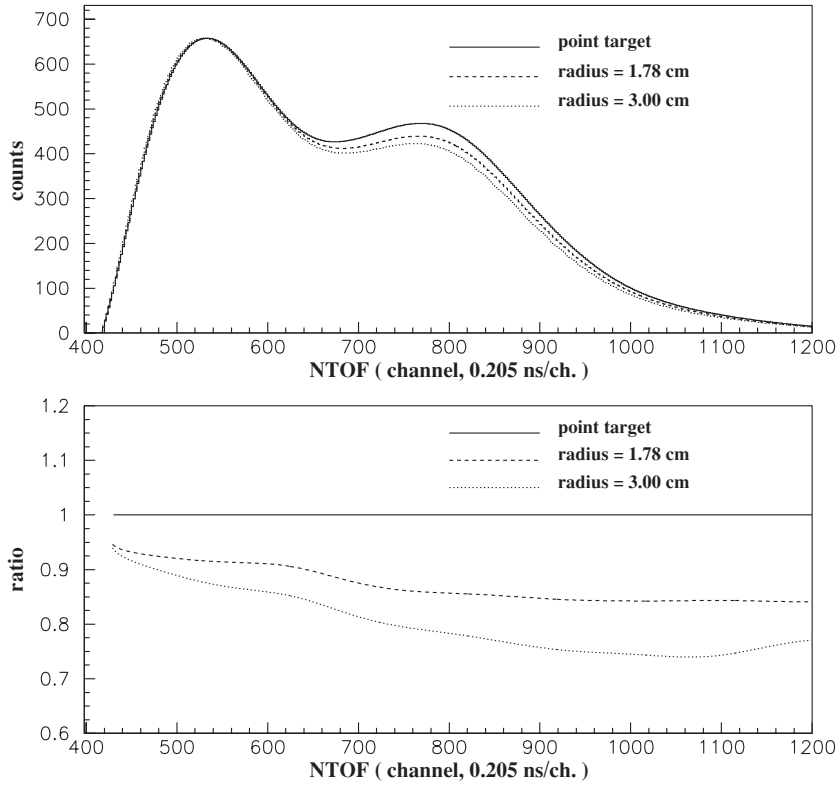

FIG. 13. Simulations showing the effects of neutron attenuation on the NTOF spectrum. (Top) NTOF spectra for three different target radii (solid curve for point target, $R = 0.00$ cm; dashed curve for $R = 1.78$ cm; and dotted curve for $R = 3.00$ cm). The spectra are normalized at the QFS peak. (Bottom) Plots of the ratio of NTOF spectra to the spectrum for the point target.

near the center of the array than for those near the edge. The contributions to the NTOF spectrum due to cross-talk events are shown in Fig. 10.

The probability for cross-talk due to $H(n, n)$ scattering in the first detector is much smaller than from $C(n, n)$ scattering because the energies of the np-scattered neutrons are typically lower than the threshold setting ($1/3\times$ Cs) of the second detector. However, for completeness cross-talk due to np scattering in the first detector was included in the simulation in the same manner as cross-talk due to nC scattering.

A separate determination of the detector cross-talk was performed at TUNL using neutrons produced by the $^2H(d, n)$ reaction. The measurements were made with 9-MeV neutrons to emulate the effects of the neutrons from $\pi^- p$ capture. The cross-talk assessment was made by placing one of the liquid scintillators from the array in the direct neutron beam and measuring the ratio of incident to detected neutrons in that scintillator under two conditions. First, the ratio was measured with that scintillator positioned alone in the neutron beam. Next, the ratio was measured with six other detectors placed adjacent to it in the same geometry as the neutron detector array used in E1286. We found that the ratio was 1.1% larger for the array arrangement.

The difference in these results and those obtained using the $^1H(\pi^-, n\gamma)$ reaction gives a measure of the systematic error in our determination of the cross-talk contribution. From the comparison of the results for these two measurements of the detector cross talk, we estimate the systematic uncertainty in our modeling of the cross-talk contribution to be $\pm 0.2\%$, which has a negligible effect in our determination of a_{nn}.

E. Simulation of the $^2H(\pi^-, n\gamma)\,n$ reaction

The experiment geometry and detector calibration parameters were determined using the $^1H(\pi^-, n\gamma)$ capture reaction. These parameters, with slight adjustments to account for the differences in the π^- beam tune between the hydrogen- and deuterium-target runs, were used as input into the $\pi^- d$ capture simulations. The stopped π^- distribution in the deuterium target was determined similarly as that for the hydrogen target by fitting the γ-ray position spectra and the θ_3 density distribution. The measured γ_x and γ_y spectra for $\theta_3 > 0.3$ radian were fit by varying the centroid of the stopped π^- distribution. For example, the chi-square (χ^2) plot for the optimization of the centroid of the stopped π^- distribution to give the fit to the γ_x spectrum is shown in Fig. 14. The uncertainty in the determination of the centroid of the vertical beam distribution was about ± 0.1 cm. Because the simulated γ_y spectra were relatively insensitive to the centroid of the stopped π^- distribution, the horizontal profile of the stopped π^- distribution used in the $\pi^- d$ simulations was taken to be the same as that obtained from the $\pi^- p$ capture data. An uncertainty of ± 0.2 cm was assigned to the horizontal position of the centroid of the stopped π^- distribution.

Neutron scattering in the target influences the shape of the NTOF spectrum and consequently the value of a_{nn} determined by fitting the measured NTOF spectrum. From the simulation, we found that the contribution to the NTOF spectrum due to in-scattering was about 4%. These findings are comparable to the values cited in Ref. [15], where the experimental setup (geometry, target size, events) was similar to ours and the

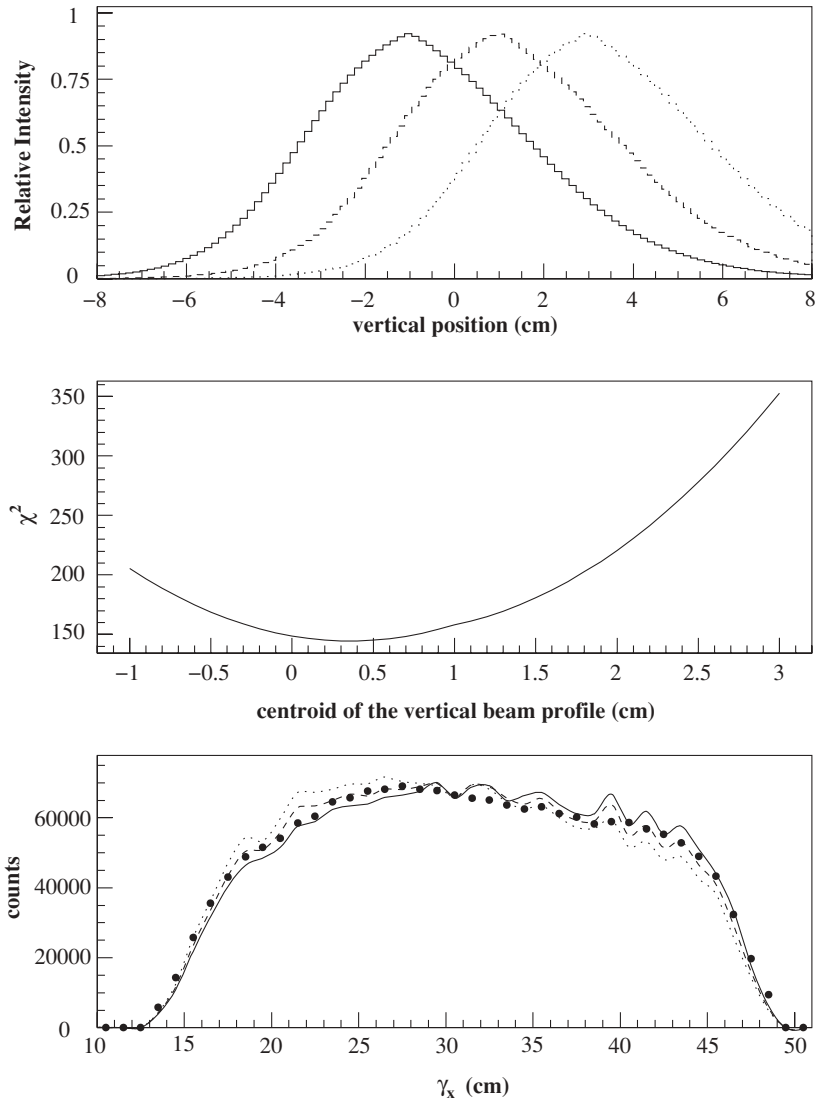

FIG. 14. Comparisons of data to MC simulations to illustrate the sensitivity of the γ_x spectrum to the centroid of the stopped π^- distribution in the deuterium target. (Top) Vertical profile of the stopped π^- distributions used in the MC simulations. (Middle) χ^2 plot for the fit to the γ_x spectrum with the vertical centroid of the stopped π^- distribution as the free parameter. (Bottom) Comparison of simulated and experimental γ_x spectrum. The bold dots are the experimental data. The solid, dashed, and dotted curves in the bottom plot are the simulated results corresponding to distributions represented by the solid, dashed, and dotted curves in the top plot, respectively.

authors claimed that 3% of the events were due to scattering in the liquid target.

The θ_3 distribution has a strong dependence on the γ-ray position at the WC and on the location of the neutron detectors. For this reason, position-dependent efficiencies in the WC and in the neutron-detector array were included in the simulations. The relative efficiencies of the neutron detectors were measured to an accuracy of $\pm 3\%$ and were included in the simulation.

The liquid deuterium target had a small hydrogen contaminant as is evident by the sharp peak in the NTOF spectrum for $\theta_3 < 0.05$ radian shown in Fig. 15. The hydrogen contamination was included in the simulations of the $\pi^- d$ capture experiment. The fractional number density of the hydrogen contamination was determined by comparing the yields from the $\pi^- d$ capture reaction to those from $\pi^- p$ capture. The simulated NTOF spectrum was normalized to the valley (channels 600 to 660) between the QFS and FSI peaks in the experimental spectrum, and the yield for π^- capture on the contaminant hydrogen in the deuterium target was obtained by subtracting the counts in the QFS peak of the normalized simulated spectrum from the counts in the same region of the measured spectrum. The hydrogen contamination in the deuterium target was found to be 0.31% by number, which is consistent with the purity specified by the deuterium gas supplier.

V. DATA ANALYSIS

A total of 70,000 double-coincidence (n-γ) and 7,000 triple-coincidence (n-n-γ) events were collected in E1286 for $\pi^- d$ capture with stopped pions. These data were accumulated in 80 production runs with the liquid deuterium target described in Sec. III. The value of a_{nn} was determined by fitting the shape of the measured NTOF for the double-coincidence events with the theoretical predictions of the model described in Sec. II. The number of triple-coincidence events was too low to obtain a statistically significant determination of a_{nn}.

The value and uncertainty of a_{nn} were determined by fitting the NTOF spectra with simulated spectra using two free parameters, a_{nn} and a normalization factor. The simulated NTOF spectra were normalized to have the same number of counts as the data in the nn FSI region between channels 650 and 1000, and the χ^2 was computed over the same region.

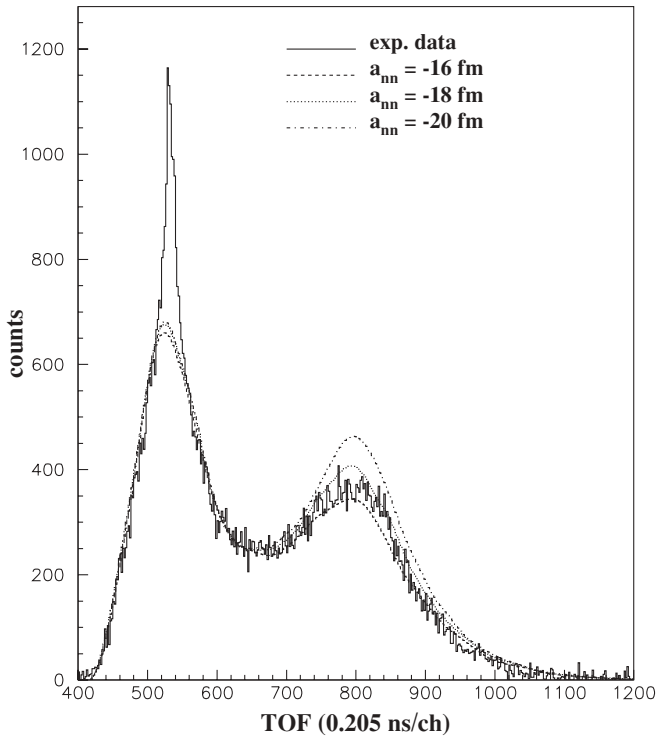

FIG. 15. Plot of NTOF spectra for the entire detector array for θ_3 cut 1 ($0 \leqslant \theta_3 \leqslant 0.05$ rad). The plot made with the bold solid curve is the experimental spectrum. The other plots are MC simulations made with $a_{nn} = -16$ fm (dashed), $a_{nn} = -18$ fm (dotted), and $a_{nn} = -20$ fm (dashed-dotted). The simulated spectra were normalized to have the same area as the experimental spectrum in the region between channels 600 and 660.

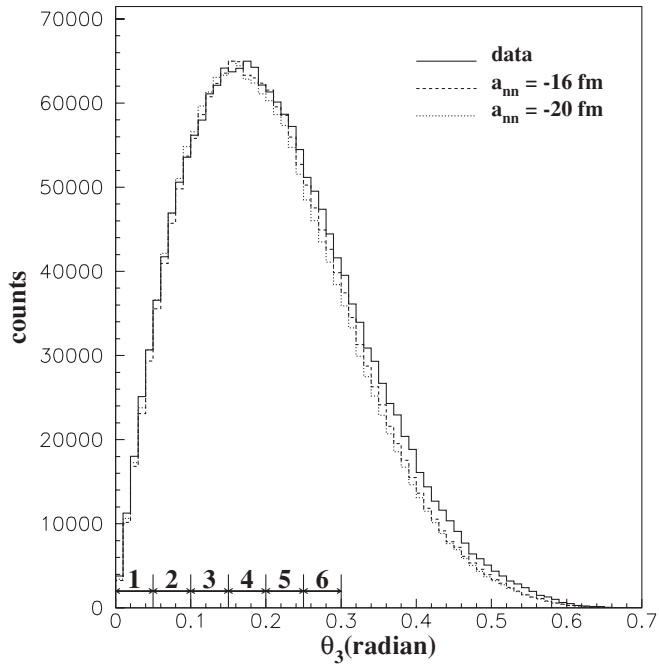

FIG. 16. Plot of the measured yields (n-γ coincidences) for π^- capture in the deuterium target as a function of θ_3. This spectrum was accumulated using the entire neutron-detector array. It contains about 98% of the total data taken in Exp1286.

The sensitivity of the shape of the NTOF spectrum to θ_3 provided a tool for diagnosing systematic errors in our techniques. Because the value of a_{nn} should be independent of the θ_3 angle, an angular dependence would indicate a systematic problem with the data, analysis technique or both. The measured yields from $\pi^- d$ capture as a function of θ_3 are shown in Fig. 16. The aggregate NTOF spectra were analyzed in 0.05-rad wide bins of θ_3 over the range $0 \leqslant \theta_3 \leqslant 0.25$ rad. The upper limit on θ_3 was set to keep the magnitude of the first term in the effective-range approximation, Eq. (2.7), a factor of 10 larger than the second term. At θ_3 angles larger than 0.25 rad the shape of the NTOF spectrum is insensitive to a_{nn} and consequently would add little to the statistical accuracy in determining a_{nn}.

The simulations were run for four values of a_{nn}, -16 fm, -18 fm, -20 fm and -22 fm. NTOF spectra corresponding to other a_{nn} values were obtained by linearly interpolating between the simulated spectra. The value of a_{nn} determined in the fit to the NTOF spectrum corresponded to the minimum χ^2 point. The statistical errors were determined from the χ^2 curve by drawing a horizontal line at the value of $\chi^2_{\min} + 1$. The a_{nn} values where the line intercepts the χ^2 curve gave the minimum and maximum values, $a_{nn}^{\min}$ and $a_{nn}^{\max}$, respectively. Our results are shown in Figs. 17–21.

VI. RESULTS AND DISCUSSION

Values of a_{nn} determined from the combined NTOF spectra of all detectors for different θ_3 bins and different MC simulations are summarized in Table I. The first column gives

TABLE I. Values of a_{nn} (fm) obtained with increasingly more realistic MC simulations. The results in this table are from the the analysis of the total-array NTOF spectrum for each θ_3 bin. The uncertainties are statistical only. The last row gives the average of the first five rows.

θ_3 Range (rad)	Point geometry	Finite geometry	Finite geom. + Scatt.	Full MC
0.00 to 0.05	-17.63 ± 0.28	-17.93 ± 0.28	-18.84 ± 0.28	-18.67 ± 0.22
0.05 to 0.10	-17.78 ± 0.28	-18.19 ± 0.28	-19.11 ± 0.28	-18.74 ± 0.17
0.10 to 0.15	-17.36 ± 0.33	-17.96 ± 0.33	-18.86 ± 0.33	-18.41 ± 0.20
0.15 to 0.20	-17.02 ± 0.28	-17.62 ± 0.28	-18.51 ± 0.37	-18.83 ± 0.24
0.20 to 0.25	-17.06 ± 0.30	-17.26 ± 0.38	-18.04 ± 0.30	-18.34 ± 0.33
Weighted average:	-17.44 ± 0.12	-17.87 ± 0.14	-18.74 ± 0.14	-18.63 ± 0.10

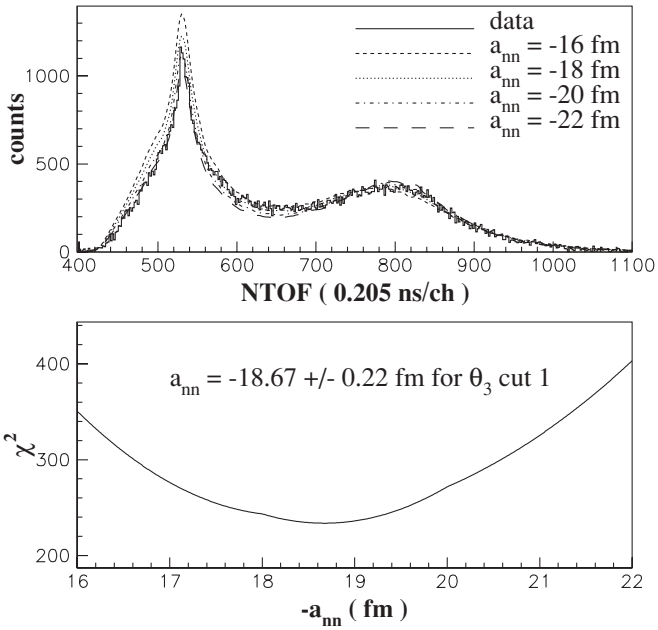

FIG. 17. The top plot is a comparison of the shape of the experimental NTOF spectrum with that of the corresponding MC simulated spectrum for θ_3 cut 1 ($0 \leqslant \theta_3 \leqslant 0.05$ rad). The spectra are for the entire neutron-detector array. The bottom plot is the total χ^2 vs. a_{nn}.

the range of θ_3 for each bin, the second gives results assuming point geometry (point target, point detectors) ignoring neutron in- and out-scattering and cross-talk between detectors, the

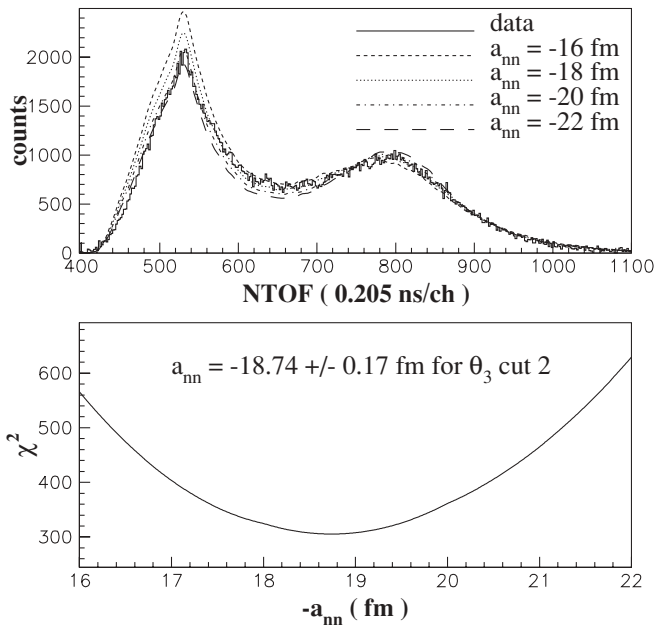

FIG. 18. The top plot is a comparison of the shape of the experimental NTOF spectrum with that of the corresponding MC simulated spectrum for θ_3 cut 2 ($0.05 \leqslant \theta_3 \leqslant 0.10$ rad). The spectra are for the entire neutron-detector array. The bottom plot is the total χ^2 vs. a_{nn}.

TABLE II. The a_{nn} values determined from the accumulated data for different types of neutron detectors for the third θ_3 bin, $0.10 < \theta_3 < 0.15$ rad. The values were obtained using the full simulation.

Detector type	a_{nn}	$\triangle a_{nn}$
A1	−18.18	0.49
A2	−18.16	0.28
B	−19.23	0.47
L	−18.48	0.60

third column gives results for finite geometry, the fourth gives results including finite geometry and neutron in- and out-scattering, and the fifth column gives the results using the full MC simulation, which includes cross-talk between detectors. The uncertainties are statistical only. The weighted average values for the first five θ_3 bins are listed at the bottom of each column. We note that the inclusion of the finite geometry makes a_{nn} more negative by about 0.4 fm, the inclusion of neutron in- and out-scattering makes it even more negative by about 1 fm. This measurement gives for a_{nn} the value of $a_{nn} = -18.63 \pm 0.10$ fm. The uncertainty is statistical only.

Now we determine a value of a_{nn} for each detector type for the third θ_3 bin of $0.10 < \theta_3 < 0.15$ rad. This bin was chosen over the other θ_3 bins analyzed because it had the largest number of counts in the *nn* FSI region of the NTOF spectrum. The a_{nn} values determined from the data for each detector type are listed in Table II. The weighted average value with statistical uncertainty of a_{nn} from Table II is

$$a_{nn} = -18.41 \pm 0.20 \text{ fm}. \tag{6.1}$$

The values of a_{nn} for three of the four detector types agree within the statistical accuracy of the measurements. We note that a_{nn} for detector type B is two standard deviations away from the average value obtained with the other three detector types. However, the values of a_{nn} obtained with the type-B detectors for other θ_3 bins are statistically consistent with the values from the other detector types. Therefore, the discrepancy between the results for the type-B detectors and the other detector types for the third θ_3 bin is likely due to statistical fluctuations.

A summary of systematic uncertainties in this experiment and in that of Ref. [15] is given in Table III. There are six significant sources of systematic error in our technique. The two sources of error that are associated with the modeling of the experiment are discussed in the next paragraph. The other four sources are discussed here. There is about a ±0.20-ns

TABLE III. Summary of systematic uncertainties (in fm) to a_{nn}.

Source of uncertainty	Ref. [15]	Present
Absolute time of flight	0.12	0.13
Background subtraction	0.16	0.01
Target vertex reconstruction	Not given	0.23
Stopped pions distribution	Not given	0.21
Detector efficiency shape	0.26	0.27
Detector bias setting	0.20	0.10

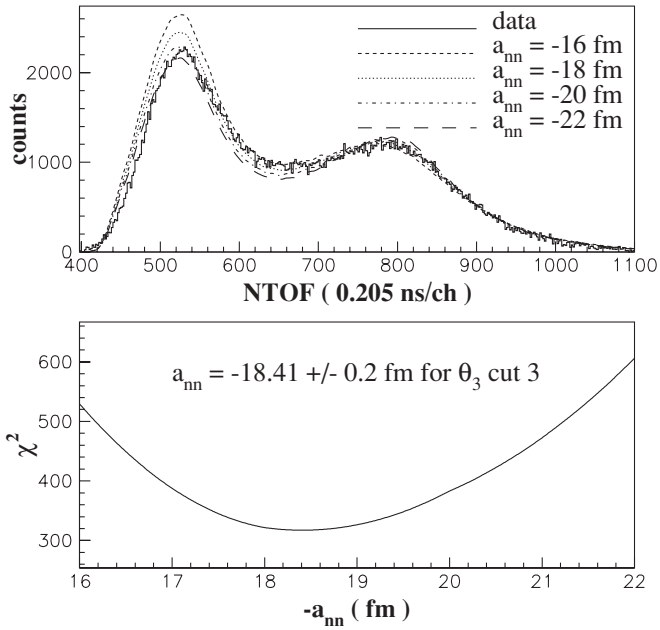

FIG. 19. The top plot is a comparison of the shape of the experimental NTOF spectrum with that of the corresponding MC simulated spectrum for θ_3 cut 3 ($0.10 \leqslant \theta_3 \leqslant 0.15$ rad). The spectra are for the entire neutron-detector array. The bottom plot is the total χ^2 vs. a_{nn}.

($\pm$ 1 channel) uncertainty in aligning the experimental NTOF spectrum for each neutron detector with the MC simulation. A shift of ± 1 channel in the simulated NTOF spectrum relative to the experimental spectrum results in a ± 0.13 fm change in the value of a_{nn}. The uncertainty in the fit to the n-γ accidental background in the NTOF spectrum gives a ± 0.01 fm uncertainty in our determination of a_{nn}. The efficiencies of the neutron detectors were measured in a separate experiment at the TUNL using a beam of neutrons from the ^{2}H(d, n) reaction and fission neutrons from a ^{252}Cf source. The ^{252}Cf was a deposit on a thin foil inside an ionization chamber. The shape of the measured efficiency curve for each detector type as a function of neutron energy was in agreement with the predictions from the PTB code [37] to within $\pm 3\%$ over the neutron energy range from 2 to 13 MeV. This uncertainty in the shape of the neutron detector efficiency curve causes a ± 0.27 fm uncertainty in the value of a_{nn} obtained in our technique. Because the shape of the neutron detector efficiency curve is very sensitive to the pulse-height threshold setting, errors in setting the detector threshold result in errors in the determination of a_{nn}. Our tolerance for setting the thresholds on the neutron detectors was 8%, i.e., allowance from the desired setting of $1/3\times$ Cs to $1/4\times$ Cs. The threshold settings on the neutron detectors were checked twice daily. The dispersion in the settings over the length of the experiment was about 4%, which is half of the precision tolerance. The data were analyzed with a threshold setting of $1/3\times$ Cs and $1/4\times$ Cs to estimate the maximum error in a_{nn} due to our precision in setting the thresholds of the neutron detectors. The difference in the values for a_{nn} obtained with the two threshold settings was ± 0.10 fm.

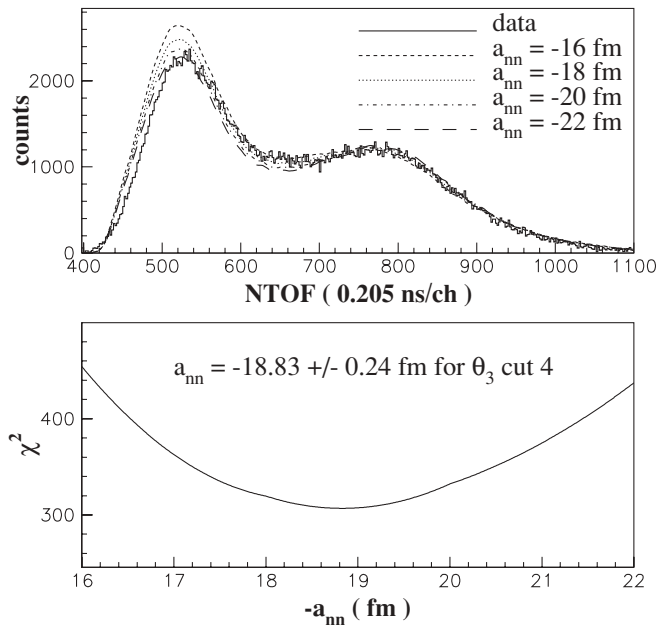

FIG. 20. The top plot is a comparison of the shape of the experimental NTOF spectrum with that of the corresponding MC simulated spectrum for a θ_3 cut 4 ($0.15 \leqslant \theta_3 \leqslant 0.20$ rad). The spectra are for the entire neutron-detector array. The bottom plot is the total χ^2 vs. a_{nn}.

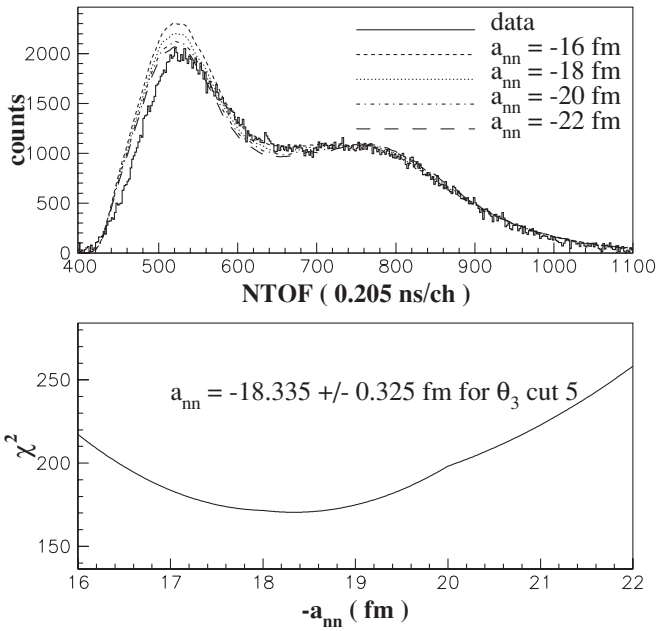

FIG. 21. The top plot is a comparison of the shape of the experimental NTOF spectrum with that of the corresponding MC simulated spectrum for θ_3 cut 5 ($0.20 \leqslant \theta_3 \leqslant 0.25$ rad). The spectra are for the entire neutron-detector array. The bottom plot is the total χ^2 vs. a_{nn}.

The high spatial resolution of the γ-ray detector enabled us to assess the systematic uncertainties in our determination of a_{nn} due to uncertainties in modeling the n-γ vertex reconstruction and the stopped pion distribution in the target. Uncertainties in the n-γ vertex reconstruction result in uncertainties in matching the experimental values of θ_3 to the values from the MC simulation. This uncertainty gives a systematic error in our determination of a_{nn} of ± 0.23 fm. We were able to determine the uncertainties in the width and centroid of the stopped pion distribution in the target by comparing the measured γ-ray position spectra to the MC simulations (see Sec. IV B). After determining the uncertainties in these parameters MC simulations were run with different values of the width and centroid of the stopped π^- distribution. With all other conditions held constant in the simulations, we found that for changes within the uncertainties in our determinations of the width and centroid of the stopped π^- distribution in the x, y, and z (incident beam axis) directions the values obtained for a_{nn} changed by 0.05, 0.10, and 0.05 fm, respectively. Assuming uncorrelated errors, the systematic uncertainty in a_{nn} is ± 0.21 fm due to our uncertainties in modeling the stopped π^- beam distribution in the target.

VII. CONCLUSION

Summing our systematic uncertainties in quadrature leads to the total systematic uncertainty of ± 0.44 fm. The estimated theoretical uncertainty is ± 0.30 fm [11,12,39]. The final value for a_{nn} from this study is $a_{nn} = -18.63 \pm 0.10 \pm 0.44 \pm 0.30$ fm $= -18.63 \pm 0.48$ fm. Results from previous studies are

$$a_{nn} = -18.60 \pm 0.34 \pm 0.26 \pm 0.30 \text{ fm} = -18.60 \pm 0.52 \text{ fm[10]}$$

and

$$a_{nn} = -18.70 \pm 0.42 \pm 0.39 \pm 0.30 \text{ fm} = -18.70 \pm 0.65 \text{ fm[15]},$$

where the last results combine all uncertainties in quadrature. Combining the results from these three studies gives a world average value obtained from $\pi^- d$ capture of $a_{nn} = -18.63 \pm 0.27 \pm 0.30$ fm and makes the total experimental uncertainty smaller than the theoretical one. When corrected for the nn magnetic interaction (which varies between 0.30 and 0.37 fm [1,22]), the world average value becomes -18.9 ± 0.4 fm, which is 1.6 ± 0.5 fm more negative than the recommended a_{pp} value. This result confirms CSB in the nucleon-nucleon $^1S_0$ state at the 1% confidence level.

ACKNOWLEDGMENTS

This work was supported in part by the US Department of Energy, Office of High Energy and Nuclear Physics, under grant DE-FG02-97ER41033, by the Duke University Research Council, by the Deutsche Forschungsgemeinschaft contract no. Me544/8-1, by the Croatian Ministry of Science Grant, by the European Community contract no. CI1*-CT-91-0894, and by the Polish Committee for Scientific Research under grant 2P03B02818.

[1] G. A. Miller, B. M. K. Nefkens, and I. Slaus, Phys. Rep. **194**, 1 (1990).
[2] D. W. Glasgow, M. S. Moore, G. L. Morgan, N. S. P. King, K. R. Alrick, M. L. Shepard, J. R. Streetman, G. M. Hale, J. H. Norman, L. R. Fawcett, C. D. Bowman, J. A. Harvey, N. W. Hill, and R. R. Spencer, Radiat. Eff. **94**, 239 (1986).
[3] W. I. Furman *et al.*, J. Phys. G: Nucl. Part. Phys. **28**, 2627 (2002); B. E. Crawford *et al.*, J. Phys. G: Nucl. Part. Phys. **30**, 1269 (2004).
[4] I. Slaus, Y. Akaishi, and H. Tanaka, Phys. Rep. **173**, 257 (1989).
[5] I. Slaus, Y. Akaishi, and H. Tanaka, Phys. Rev. Lett. **48**, 993 (1982).
[6] L. Aamondt *et al.*, Phys. Rev. **83**, 1057 (1951); K. M. Watson and R. N. Stuart, *ibid.* **82**, 738 (1951); R. H. Phillips and K. M. Crowe, *ibid.* **96**, 484 (1954).
[7] R. P. Haddock, R. M. Salter, Jr., M. Zeller, J. B. Czirr, and D. R. Nygren, Phys. Rev. Lett. **14**, 318 (1965).
[8] R. M. Salter, Jr, R. P. Haddock, M. Zeller, D. R. Nygren, and J. B. Czir, Nucl. Phys. **A254**, 241 (1975).
[9] C. R. Howell, Q. Chen, T. S. Carman, A. Hussein, W. R. Gibbs, B. F. Gibson, G. Mertens, C. F. Moore, C. Morris, A. Obst, E. Pasyuk, C. D. Roper, F. Salinas, I. Slaus, S. Sterbenz, W. Tornow, R. L. Walter, C. R. Whiteley, and M. Whitton, Phys. Lett. **B444**, 252 (1998).
[10] B. Gabioud, J. C. Alder, C. Joseph, J.-F. Loude, N. Morel, A. Perrenoud, J. P. Perroud, M. T. Tran, E. Winkelmann, W. Dahme, H. Panke, D. Renker, C. Zupancic, G. Strassner, and P. Truol, Phys. Rev. Lett. **42**, 1508 (1979); B. Gabioud, J. C. Alder, C. Joseph, J.-F. Loude, N. Morel, A. Perrenoud, J. P. Perroud, M. T. Tran, E. Winkelmann, W. Dahme, H. Panke, D. Renker, G. Strassner, P. Truol, and G. F. de Téramond, Phys. Lett. **B103**, 9 (1981); Nucl. Phys. **A420**, 496 (1984).
[11] W. R. Gibbs, B. F. Gibson, and G. J. Stephenson, Jr, Phys. Rev. C **11**, 90 (1975).
[12] W. R. Gibbs, B. F. Gibson, and G. J. Stephenson, Jr, Phys. Rev. C **12**, 2130 (1975).
[13] G. F. de Téramond, Phys. Rev. C **16**, 1976 (1977).
[14] M. Bander, Phys. Rev. **134**, B1052 (1964).
[15] O. Schori, B. Gabioud, C. Joseph, J. P. Perroud, D. Rüegger, M. T. Tran, P. Truöl, E. Winkelmann, and W. Dahme, Phys. Rev. C **35**, 2252 (1987).
[16] C. R. Howell, *Proceedings of the X International Seminar on Interactions of Neutrons with Nuclei, Dubna, Russia, ISINN-10 (2003)*, p. 71; arXiv: 0805.1177v1 [nucl-ex].
[17] W. Tornow, R. T. Braun, and H. Witała, Phys. Lett. **B318**, 281 (1993); H. Witała, J. Golak, W. Tornow, W. Glöckle, and D. Hüber, Phys. Rev. C **51**, 1095 (1995); W. Tornow, R. T. Braun, H. Witała, and N. Koori, Phys. Rev. C **54**, 42 (1996); W. Tornow, H. Witała, and R. T. Braun, Few-Body Syst. **21**, 97 (1996).
[18] W. von Witsch, X. Ruan, and H. Witała, Phys. Rev. C **74**, 014001 (2006).
[19] D. E. González Trotter, F. Salinas, Q. Chen, A. S. Crowell, W. Glöckle, C. R. Howell, C. D. Roper, D. Schmidt, I. Slaus, H. Tang, W. Tornow, R. L. Walter, H. Witała, and Z. Zhou, Phys. Rev. Lett. **83**, 3788 (1999).

[20] V. Huhn, L. Wätzold, Ch. Weber, A. Siepe, W. von Witsch, H. Witała, and W. Glöckle, Phys. Rev. Lett. **85**, 1190 (2000).
[21] R. J. Slobodrian, Phys. Lett. **B135**, 17 (1984).
[22] H. Witała, J. Golak, R. Skibiński, C. R. Howell, and W. Tornow, Phys. Rev. C **67**, 064002 (2003).
[23] M. Przyborowski, M. Eggert, R. Engels, M. Menzel, L. Sydow, H. P. gen. Schieck, H. Witała, J. Golak, J. Kuroś, and W. Glöckle, Phys. Rev. C **60**, 064004 (1999); H. Brückmann, W. Kluge, H. Mathäy, L. Schänzler, and K. Wick, Nucl. Phys. **A157**, 209 (1970).
[24] C. R. Howell, Nucl. Phys. **A689**, 298c (2001).
[25] V. Ajdacic, M. Cerineo, B. Lalovic, G. Paic, I. Slaus, and P. Tomas, Phys. Rev. Lett. **14**, 444 (1965); D. R. Tilley, H. R. Weller, and H. H. Hasan, Nucl. Phys. **A474**, 1 (1987).
[26] D. V. Aleksandrov, E. Yu Nikol'skii, B. G. Novatskii, and D. N. Stepanov, JETP Lett. **59**, 320 (1994).
[27] H. Witała and W. Glöckle, Phys. Rev. C **60**, 024002 (1999) and references therein.
[28] K. M. Watson and R. N. Stuart, Phys. Rev. **82**, 738 (1951).
[29] K. W. McVoy, Phys. Rev. **121**, 1401 (1961).
[30] G. F. Chew, M. L. Goldberger, F. E. Low, and Y. Nambu, Phys. Rev. **106**, 1345 (1957).
[31] M. Leon, Phys. Lett. **B37**, 87 (1971).
[32] M. Krell and T. E. O. Ericson, Nucl. Phys. **B11**, 521 (1969).
[33] H. S. Picker and E. F. Redish, Phys. Rev. C **8**, 2495 (1973).
[34] R. L. Fulton, *Mechanic Design of the LAMPF Low-Energy Pion Channel*, LA-5222-MS, Informal Report UC 34 & 38, LAMPF, Los Alamos, Nex Mexico 87544, 1973 (unpublished).
[35] M. Drosg, Nucl. Sci. Eng. **67**, 190 (1978).
[36] G. Dietze and H. Klein, *NRESP4 and NEFF4 Monte Carlo Codes for the Calculation of Neutron Response Functions and Detection Efficiencies for NE 213 Scintillation Detectors*, Technical Report PTB-ND-22, Physikalisch-Technische Bundesanstalt, Bundesallee 100, W-3300 Braunschweig, 1982 (unpublished).
[37] M. Tichy, H. Klein, and J. Pulpan, *Calibration of an NE-213 Scintillator*, Technical Report PTB-7.2-92-1, Physikalisch-Technische Bundesanstalt, Bundesallee 100, W-3300 Braunschweig, 1992 (unpublished).
[38] R. L. Boudrie, J. L. Matthews, and C. L. Morris, Los Alamos National Laboratory Report No. LA-UR-91-1847, 1991 (unpublished); J. D. Bowman, in *Pion-Nucleus Physics: Future Directions and New Facilities at LAMPF*, edited by R.J. Peterson and D. D. Strottman, AIP Conf. Proc. No. 163 (AIP, New York, 1988), p. 119.
[39] B. F. Gibson (private communication, 1997).